Single-cell characterization of human GBM reveals regional differences in tumor-infiltrating leukocyte activation

Philip Schmassmann[1,*], Julien Roux[2,3], Steffen Dettling[4], Sabrina Hogan[1], Tala Shekarian[1], Tomás A. Martins[1], Marie-Françoise Ritz[1], Sylvia Herter[5], Marina Bacac[5], and Gregor Hutter[1,6,*]

[1]Brain Tumor Immunotherapy Lab, Department of Biomedicine, University of Basel, Basel, Switzerland

[2]Bioinformatics Core Facility, Department of Biomedicine, University of Basel, Basel, Switzerland

[3]Swiss Institute of Bioinformatics, Basel, Switzerland

[4]Roche Pharmaceutical Research and Early Development, Roche Innovation Center Munich, Penzberg, Germany

[5]Roche Pharmaceutical Research and Early Development, Roche Innovation Center Zürich, Schlieren, Switzerland

[6]Department of Neurosurgery, University Hospital Basel, Basel, Switzerland

[*]Correspondence: p.schmassmann@unibas.ch, gregor.hutter@usb.ch

Abstract

Glioblastoma (GBM) harbors a highly immunosuppressive tumor microenvironment (TME) which influences glioma growth. Major efforts have been undertaken to describe the TME on a single-cell level. However, human data on regional differences within the TME remain scarce. Here, we performed high-depth single-cell RNA sequencing (scRNAseq) on paired biopsies from the tumor center, peripheral infiltration zone and blood of five primary GBM patients. Through analysis of > 45'000 cells, we revealed a regionally distinct transcription profile of microglia (MG) and monocyte-derived macrophages (MdMs) and an impaired activation signature in the tumor-peripheral cytotoxic-cell compartment. Comparing tumor-infiltrating $CD8^+$ T cells with circulating cells identified $CX3CR1^{high}$ and $CX3CR1^{int}$ $CD8^+$ T cells with effector and memory phenotype, respectively, enriched in blood but absent in the TME. Tumor $CD8^+$ T cells displayed a tissue-resident memory phenotype with dysfunctional features. Our analysis provides a regionally resolved mapping of transcriptional states in GBM-associated leukocytes, serving as an additional asset in the effort towards novel therapeutic strategies to combat this fatal disease.

35 **Introduction**

36 Glioblastoma (GBM) is a fatal disease without effective long-term treatment options.
37 The current standard of care consists of tumor resection followed by adjuvant chemoradiother-
38 apy resulting in a median overall survival of only 14 months [1]. One of the hallmarks in GBM
39 progression is the high rate of neovascularization. The GBM-induced aberrant vessels not only
40 nourish glioma cells, but also provide a specialized niche for tumor-associated stromal and im-
41 mune cells such as monocyte-derived macrophages (MdMs), yolk sac-derived microglia (MG)
42 (together termed glioma-associated macrophages/microglia, GAMs), and peripheral adaptive
43 immune cells. This immune tumor microenvironment (iTME) paradoxically acts in an immu-
44 nosuppressive manner and promotes tumor progression [2]. For example, clinical trials of sys-
45 temic T cell checkpoint blockade showed only disappointing results [3, 4], which was attributed
46 in part to the immunosuppressive components of the GBM iTME. The origin of GAMs, infil-
47 tration of peripherally derived macrophages across the blood-brain-barrier (BBB) or recruit-
48 ment of tissue-resident MG to the tumor site, as well as their contribution to gliomagenesis are
49 studied intensively [2, 5-7]. Hence, major efforts have been undertaken to describe the GBM
50 iTME on a single cell level [5, 6, 8], or dissect the composition and changes upon disease stages,
51 recurrence and immunotherapy specifically within the GAM compartment [9-11]. However,
52 human data on the composition of the iTME in different tumor regions (contrast enhancing
53 tumor center versus peripheral infiltration zone) remain scarce [12, 13].

54 To study the region-dependent cellular diversity within individual GBMs, we performed
55 single-cell RNA sequencing (scRNA-seq) on patient-matched biopsies from the tumor center
56 and the peripheral infiltration zone of five primary GBM patients. Additionally, peripheral
57 blood mononuclear cells (PBMC) of the same patients were included to explore the transcrip-
58 tional changes occurring during tumor infiltration of circulating immune cells.

59 Our analysis revealed a regionally distinct transcription profile of MG and MdMs and
60 an impaired activation signature in the tumor-peripheral cytotoxic-cell compartment. Compar-
61 ing tumor-infiltrating $CD8^+$ T cells with PBMC-derived, identified $CX3CR1^{high}$ and $CX3CR1^{int}$
62 $CD8^+$ T cells with effector and memory phenotype, respectively, enriched in blood but absent
63 in the iTME. Tumor $CD8^+$ T cells displayed features of tissue-resident memory T cells and
64 were characterized by an exhaustion phenotype. This work provides a regionally-resolved map
65 of transcriptional states in glioma-associated cell types complemented by patient-matched
66 PBMCs, dissecting the composition and molecular diversity of the iTME in GBM.

Results

scRNA-seq analysis of paired tumor center, periphery and PBMC samples.

Fresh, neurosurgically resected tissue from five primary, treatment naïve GBM patients were harvested (Figure 1A, Supplementary File 1). According to the 2021 WHO Classification of Tumors of the Central Nervous System [14], in which the term glioblastoma designates only IDH-wildtype grade 4 tumors, we will hence use the term grade 4 glioma, as we included as well IDH-mutant grade 4 tumors (Supplementary File 1). The tumor center was defined as contrast enhancing, whereas the tumor periphery was defined as T2 hyperintense by magnetic resonance imaging (MRI)-guided, navigated surgical resection (Figure 1B). Increased cellular density of the center vs. periphery samples was confirmed by nuclear DAPI staining on matched histological micrographs of the resected tissue specimens used for scRNA-seq (Figure 1C). As outlined in Figure 1A, we separately processed patient tumor and blood samples and enriched them for immune cells by fluorescence-activated cell sorting (FACS) (Figure 1 – figure supplement 1A and 1B). The three samples per patient (center, periphery and PBMC) were loaded on different wells of a 10x Genomics Chromium system for a targeted recovery of 10,000 cells. Due to technical issues cells from the center sample of patient BTB 609 could not be collected.

In total we analyzed 45,466 cells that passed initial quality control and filtering, comprising 8,254 cells from tumor center, 5,954 cells from tumor periphery and 31,258 PBMCs, with 6,354 to 10,957 cells per patient (Supplementary File 2; Figure 1 – figure supplement 1C-1E, Supplementary File 3). All cells were projected onto a two dimensions *t*-distributed stochastic neighbor embedding (tSNE) [15]. As we observed a good overlap of cells across patients for most of the dataset (see Methods) (Figure 1 – figure supplement 2B – 2F), we chose not to perform any correction for patient-specific effects. Using hierarchical clustering, the cells were partitioned into clusters (Figure 2 – figure supplement 1A, 1B) which were then annotated into nine distinct cell types for the immune subset, including two transcriptionally distinct MG subsets (MG_1 and MG_2) and four cell types for the CD45 negative subset (Figure 2A; Figure 2 – figure supplement 1C, 1D; Supplementary File 3).

In more detail, our annotation strategy made use of the relative expression patterns of known marker genes (Figure 2B), and of cluster-specific genes (Figure 2 – figure supplement 2). Additionally, unbiased cell-type annotation using whole-transcriptome comparisons to reference bulk and single-cell datasets was performed with the *SingleR* package. We used as reference (i) a public bulk RNA-seq dataset of sorted immune cell types from human PBMC samples [16], which helped in identifying the major immune cell lineages: B cells, $CD4^+$ and $CD8^+$ T cells, dendritic cells (DCs), monocytes and NK cells (Figure 2 – figure supplement 1E). (ii)

101 A bulk RNA-seq dataset of sorted immune cell types from the TME of human gliomas [5] was
102 helpful to separate GBM-associated $CD4^+$ and $CD8^+$ T cells, as well as microglia and MdMs
103 (Figure 2 – figure supplement 1F). (iii) A 10X genomics scRNA-seq dataset of the innate im-
104 mune TME of seven newly diagnosed GBM patients [9] confirmed the annotation of the innate
105 immune subset (Figure 2 – figure supplement 1I), which was also supported by a microglia and
106 a macrophage signature scores defined using gene lists obtained from [7] (Figure 2 – figure
107 supplement 1J, 1K). (v) Finally a Smartseq2 scRNA-seq dataset of *IDH1*^{wt} tumors [17] was
108 used to characterize the $CD45^{neg}$ population (Figure 2 – figure supplement 1N).
109 To perform a differential expression analysis between tumor sites, we stratified the anal-
110 ysis by cell type to decrease the influence of differential abundance patterns (analyzed sepa-
111 rately, see below). A principal component analysis (PCA) on the pseudo-bulk aggregated sam-
112 ples (see Methods) confirmed that the major source of variation was due to differences between
113 lymphoid, MG/myeloid cells, and $CD45^-$ cells (PCs 1 and 2; Figure 2C). There was no clear
114 association to the *IDH1* status of patients on these or deeper components. However, our study
115 was neither designed nor powered to find regional signatures within the iTME depending on
116 *IDH1* status, but rather to identify common transcriptional differences within the iTME be-
117 tween tumor center, periphery and PBMC of *IDH1*^{wt} and *IDH1*^{mut} grade 4 glioma.
118 Differential abundance analysis between tumor center and periphery did not reveal sig-
119 nificant changes, but some populations displayed suggestive differences: the abundance of both
120 $CD4^+$ T cell and monocytic clusters increased in periphery compared to center, while the abun-
121 dance of MdM clusters decreased (Figure 2D). This has been observed by others as well [12,
122 18]. Testing the abundance at a finer scale with *miloR* provided us interesting insights. Indeed,
123 within the innate immune population (Figure 2E) we confirmed the decreased abundance of
124 MdMs in the tumor periphery and noticed an increased abundance of the MG_1 subset of MG
125 in the tumor periphery. (Figure 2F, 2G).
126
127 *MG display regionally resolved transcriptional profiles that differ from those of DCs and*
128 *MdMs.*
129 Differential expression analysis between MG from tumor center and periphery revealed
130 downregulation of inflammatory-related genes in the peripheral MG (*FCGBP* and *CCL20*),
131 downregulation of genes associated with canonical interferon (IFN) responses (*IFI6, IFI27,*
132 *STAT1, ISG15)*, and cell proliferation (*STMN1*) as well as downregulation of scavenger receptor
133 gene *CD163* (Figure 3A and Supplementary File 4). The latter was shown to have a potential

role in the phagocytic response of MG to beta-amyloid depositions identified in single-nucleus RNA-seq of postmortem human brain[19].

Among many upregulated genes whose function is not yet known, we found Inhibitor of DNA-Binding 1, also known as Inhibitor of Differentiation 1 (*ID1*) to be increased in the peripheral MG (Figure 3A). ID1 is well described in GBM progression, treatment resistance and glioma stem cell biology [20]. However, new evidence has emerged, linking *ID1* to suppression of the anti-tumor immune response in the myeloid compartment and promoting tumor progression [21].

To further explore the underlying biological processes differing between MG in the two compartments, we conducted a gene set enrichment analysis (GSEA) on the results of the differential expression analysis using Gene Ontology (GO) database (Biological Processes). This revealed overall a significant downregulation of GO categories involved in antigen processing and presentation via MHC-I and MHC-II in the peripheral MG relative to the center MG, as well as downregulation of amino acid metabolism and TNF-α signaling pathway (Figure 3B), which supported the conclusion of an impaired activation state of peripheral MG.

When comparing the transcriptional profiles of the other innate immune phagocytic populations, DCs and MdMs, we observed for both cell types upregulation of pro-inflammatory related gene sets in the tumor periphery compared to tumor center (Figure 3C, 3D, Figure 3 - figure supplement 1A, 1B and Supplementary File 4). Within DCs, the induced pro-inflammatory phenotype was also observed when comparing DCs from tumor periphery to PBMC-derived ones (Figure 3 -figure supplement 1C, 1D and Supplementary File 6). Taken together, DCs and MdMs seem to have a proinflammatory phenotype in the glioma periphery as opposed to MG. However, they are less abundant there, at least as far as MdMs are concerned (Figure 2E-2G).

The iTME of grade 4 glioma harbors two transcriptionally distinct MG subpopulations.

Unsupervised hierarchical sub-clustering of the MG population revealed two transcriptionally distinct iTME MG subsets, which we termed MG_1 and MG_2, respectively (Figure 3E, Figure 3 – figure supplement 1E and Supplementary File 5). The MG_1 cluster was highly enriched for the activator protein-1 (AP-1) family of transcription factors including *FOS, FOSB, JUN, JUNB, MAF* and *MAFB* (Figure 3F and Supplementary File 5), which convey a surveilling phenotype to adult MG, but are also involved in numerous processes including cell growth, differentiation and immune activation [22]. Specifically, *FOSB* gene products were implicated in the excitotoxic MG activation by regulating complement C5a receptor expression

168 [23]. Yet, concomitant upregulation of anti-inflammatory Krüppel-like factor 2 (*KLF2*) [24]
169 and Dual Specificity Protein Phosphatase 1 (*DUSP1*), an inhibitor of innate inflammation by
170 negatively regulating the mitogen-activated protein kinase (MAPK) pathway [25], together
171 with increased expression of anti-proliferative genes like *RHOB, BTG1* and *BTG2* paint a more
172 complex picture of these cells. Particularly, *BTG1* was identified as an activation-induced apop-
173 totic sensitizer in MG after exposure to inflammatory stimuli [26], serving as an autoregulatory
174 mechanism and possibly hinting towards an exhausted state in these MG_1 cells. GSEA for
175 differences between MG_1 and MG_2 clusters using the MSigDB Hallmark collection of major
176 biological pathways [27] revealed downregulation of many MG effector functions in the MG_1
177 population including (1) inflammation ("Complement", "Allograft Rejection", "Reactive Oxy-
178 gen Species Pathway"), (2) immune cell activation ("IFN-α Response", "IFN-γ Response",
179 "IL6 JAK STAT3 Signaling") and (3) immunometabolism ("Fatty Acid Metabolism", Oxida-
180 tive Phosphorylation", "Glycolysis") (Figure 3G). As we examined the expression of previ-
181 ously described reactivity markers of MG including *C1QA*, *FCGR1A, CD14, HLA-DRA*,
182 *TREM2 and* Ferritin (*FTH1*) [28-31] (Figure 3H and Figure 3 – figure supplement 1F), and
183 established MG homeostatic genes like *CX3CR1, HEXB* and *SPI1* (PU.1) (Supplementary File
184 5), we noted a reduced expression of these genes in the MG_1 cluster compared to MG_2 cells,
185 while the anti-inflammatory transcription factors *NR4A1* [32] *NR4A2* [33] were highly upreg-
186 ulated (Figure 3 – figure supplement 1G). Additionally, when comparing the distribution of
187 MG subsets between sites among total MG, we observed an increased abundance of MG_1
188 cells in the tumor periphery, which might at least partially explain the previously observed
189 impaired activation state of total peripheral MG (Figure 3 – figure supplement 1H). To rule out
190 this explanation we stratified the differential expression analysis between tumor periphery and
191 center by MG subtype and observed similar genes downregulated in the tumor periphery in
192 each subtype (e.g. *CCL20, FCGBP*) (Supplementary File 5), arguing that the non-reactive phe-
193 notype is a common feature for all peripheral MG and is not only driven by a differential abun-
194 dance pattern of one MG subpopulation relative to the other.
195
196 *The tumor peripheral cytotoxic cell compartment exhibits an impaired activation signature.*
197 Next, we investigated the regional differences in the lymphoid compartment composed
198 of $CD4^+$ and $CD8^+$ T cells and natural killer (NK) cells. We observed only very few significant
199 changes in the transcriptomic profiles of $CD4^+$ T cells between tumor center and periphery
200 (Figure 4 – figure supplement 1A and Supplementary File 4). Yet, comparing peripheral $CD8^+$
201 T cells with $CD8^+$ T cells from tumor center revealed 110 differentially expressed genes (43

genes upregulated and 67 genes downregulated) (Figure 4A and Supplementary File 4). Many downregulated genes in the peripheral CD8$^+$ T cells associated with canonical IFN responses (*IFI6, IFI27, MX1, STAT1, EPSTI1 PARP9, ISG15)* [34] cell proliferation (*STMN1, CENPF, HELLS, NUSAP1* and *DNPH1*) and T cell co-stimulation (*CD28, TMIGD2* (CD28H), *TNFRSF4* (OX40), *CD27* and *TNFRSF18* (GITR)) (Figure 4A). Contrary to our expectations, we saw upregulation of *CTLA4* in the center CD8$^+$ T cells which acts as a negative costimulatory molecule. However, unlike other costimulatory receptors, such as CD27 and CD28*,* CTLA-4 is not constitutively expressed on T lymphocytes [35]. but only induced following T cell activation, along with positive costimulatory molecules such as OX40 and GITR. In addition, upregulation of CTLA-4 requires entry into the cell cycle [35]. In line with that, we detected an upregulation of proliferative genes in center CD8$^+$ T cells. In summary, CTLA-4 induction in center CD8$^+$ T cells rather suggested T cell activation than exhaustion, especially since other inhibitory receptors like *PDCD1* (PD-1)*, LAG3* and *HAVCR2* (TIM-3) were not differentially expressed between sites. Moreover, we did not observe differential expression of genes involved in CD8$^+$ T cell effector functions like cytotoxicity (e.g., *GZMK, GZMB, KLRG1,* PRF1) or cytokines (e.g., *CCL5, XCL1, XCL2, IL10*)*.* Yet, we noted upregulation of inhibitory genes (*TGFB1* and *FCRL6* [36]) in the peripheral CD8$^+$ T cells, suggesting that a pool of activated, proliferating and IFN-responsive CD8$^+$ T cells is present in the tumor center, however, absent in the tumor periphery.

Similar trends were observed for the peripheral NK cell population with peripherally reduced IFN response (*MX1* and *IFI44L*), and proliferative genes (*STMN1, HELLS, CENPF, PTTG1* and *DNPH1*), downregulated stimulatory receptors (*TMIGD2* (CD28H) and *TNFRSF18* (GITR)), and reduced NF-κB signaling (*NFKB1* and *RELB*) (Figure 4B and Supplementary File 4). Although, we observed upregulation of key genes associated with NK cell effector function in the periphery (e.g., *FCGR3A* (CD16), *FGFBP2, ITGB2, GZMH* and *KIR2DS4*), increased expression of inhibitory receptors like *LILRB1* and *KLRG1*, the latter especially in co-expression with chemokine receptor *CX3CR1*, identified the peripheral NK cells rather to be terminally differentiated with impaired cytotoxic capabilities [37]. This was in line with the observed abrogated cytokine activity profile in the peripheral NK cells with reduced expression of key factors like *XCL1, XCL2, LTB* and *CKLF.* In summary, our data revealed an impaired activation signature in the peripheral cytotoxic cell compartment.

CX3CR1 labels a specific CD8$^+$ T cell population in the circulation of grade 4 glioma patients.

235 Next, we investigated the relationships between circulating $CD8^+$ T cells and those from
236 the tumor milieu and, more specifically, the peripheral, infiltration zone characterized by an
237 abrogated $CD8^+$ T-cell IFN response and activation signature. Strikingly, there were large tran-
238 scriptomic differences between PBMC and periphery $CD8^+$ T cells (Figure 5A), with 1,417
239 differentially expressed genes (864 genes upregulated in the tumor periphery and 553 genes
240 upregulated in PBMC) (Figure 5B, Supplementary File 6).
241 Interestingly, one of the key genes upregulated in PBMC $CD8^+$ T cells was the chemo-
242 kine receptor *CX3CR1* (Figure 5B). Flow cytometry of an additional matched glioma grade 4
243 patient cohort confirmed an increased abundance of $CX3CR1^+$ $CD8^+$ T cells in PBMC com-
244 pared to almost absent $CX3CR1^+$ $CD8^+$ T cells in tumor periphery (Figure 5C, Figure 5 – figure
245 supplement 1A, Supplementary File 1). Unsupervised hierarchical sub-clustering of $CD8^+$ T
246 cells revealed that *CX3CR1* expression labelled a specific subpopulation among PBMC $CD8^+$
247 T cells (Figure 5D, 5E).
248 Recently, expression of CX3CR1 was demonstrated to distinguish memory $CD8^+$ T cells
249 with cytotoxic effector function in healthy donors and different inflammation related conditions
250 [38-41]. Further characterization of classical central memory (T_{cm}) and effector memory (T_{em})
251 populations by varying surface expression levels of CX3CR1 identified a novel $CX3CR1^{int}$
252 subpopulation, termed peripheral memory (T_{pm}). T_{pm} cells underwent frequent homeostatic di-
253 visions, re-acquired CD62L, homed to lymph nodes, and predominantly surveyed peripheral
254 tissues compared to T_{cm} and T_{em} [39]. In our dataset, the circulating $CX3CR1^+$ $CD8^+$ T cells
255 indeed displayed a core signature of memory $CD8^+$ T cells with effector function, comprising
256 expression of LFA-1 (*IGAL- ITGB2*), *TBX2* (Tbet), *SELL* (CD62L), *GZMB* (Granzyme B) and
257 *PRF1* (Perforin 1) (Figure 5F), separating them from circulating $CX3CR1^-$ $CD28^{high}$, $IL7R^{high}$
258 and $CD27^{high}$ naïve $CD8^+$ T cells (Figure 5G and Figure 5 – figure supplement 1B). Flow cy-
259 tometric analysis confirmed T_{eff} to be $CX3CR1^{high}$, with negligible expression levels in the na-
260 ïve $CD8^+$ T cells, whereas the identified memory $CD8^+$ T cells (T_{em} and T_{pm}) were $CX3CR1^{int}$
261 (Figure 5H, 5I). Collectively, surface expression analysis of CX3CR1 identified a subset of
262 $CX3CR1^{high}$ T_{eff} and $CX3CR1^{int}$ memory (T_{em}, T_{pm}) $CD8^+$ T cells in the circulation of grade 4
263 glioma patients with potentially elevated tissue surveilling properties in the case of T_{pm}, which
264 are, however, largely absent in the tumor microenvironment.
265
266 *$CD8^+$ T cells in the tumor periphery share features with tissue-resident memory T cells (T_{rm})*
267 We next examined the differing transcriptional and surface-specific features between
268 tumor infiltrating and circulating $CD8^+$ T cells. Surface staining for CD45RA and CD45RO,

269 discriminating naïve/effector from memory T cells, attributed a predominant CD45RO$^+$
270 memory phenotype to the tumor infiltrating CD8$^+$ T cells (Figure 6A, 6B). Interrogation of the
271 transcriptomic profile of these cells revealed a key marker expression signature consistent with
272 tissue-resident memory T cells (T_{rm}): Expression of cellular adhesion molecules (integrins)
273 *ITGA1* (CD49a) and *ITGAE* (CD103), tissue retention marker *CD69*, chemokine receptors im-
274 plicated in tissue-homing *CXCR3, CXCR6* and *CCR5* [42] and transcription factors, *ZNF683*
275 (Hobit) and *PRDM1* (Blimp1) as well as reduced expression of *TBX21* (Tbet) and *EOMES* [43],
276 strongly suggested a T_{rm} phenotype for these cells (Figure 6C, 6D and Figure 6 – figure sup-
277 plement 1A). Co-expression analysis of paired PBMC and tumor periphery samples using flow
278 cytometry showed that CD69$^+$ CD103$^-$ and CD69$^+$ CD103$^+$ cells are the dominant CD8$^+$ T cell
279 populations in the tumor periphery (Figure 6E, 6F). Combined, these data strongly suggest a
280 T_{rm} phenotype for the CD8$^+$ T cells in the tumor periphery.
281 Previous reports of T_{rm} populating the brain in the aftermath of central or peripheral
282 infections concluded that brain T_{rm} cells surveil the brain tissue and mediate protection by rapid
283 activation and enhanced cytokine production [42]. Indeed, CD8$^+$ T cells in the tumor periphery
284 showed increased expression of genes belonging to costimulatory pathways, including *ICOS,*
285 *TNFRSF4* (OX40) and *TNFRSF9* (4-1BB) (Figure 6 – figure supplement 1B, Supplementary
286 File 6), albeit accompanied by high levels of inhibitory receptors *PDCD1* (PD-1), *LAG3,*
287 *HAVCR2* (TIM-3) and *CTLA4* (Figure 6G). Moreover, expression of genes coding for cytotoxic
288 molecules, including Granzyme B and Perforin 1 were decreased in the peripheral CD8$^+$ T cells,
289 suggesting a compromised killing capacity of these cells. And lastly, CD8$^+$ T cells in the tumor
290 periphery exhibited a transcription factor profile of exhausted T cells with high expression of
291 *NR4A1, MAF* and *IRF4* (Figure 6G and Figure 6 – figure supplement 1C), which were impli-
292 cated in T cell dysfunction and exhaustion [44, 45]. Collectively, these data indicate that CD8$^+$
293 T cells in the glioma periphery share features with T_{rm} cells. However, inhibitory receptor ex-
294 pression, functional molecules and transcriptional signature ascribe an exhausted phenotype to
295 these cells.
296 Noteworthy, we observed high upregulation of similar genes in the comparison tumor
297 periphery vs. PBMC for CD4$^+$ T cells as for CD8$^+$ T cells (Figure 6 – figure supplement 1D).
298 These included transcription factor family *NRA41-3,* identified as key mediator of T cell dys-
299 function [45], Dual Specificity Protein Phosphatase 2/4 (*DUSP2, DUSP4*) described as nega-
300 tive regulators of mitogen-activated protein (MAP) kinase superfamily and associated with im-
301 paired T cell effector activity [46] and T cell senescence [47], and transcription factor *CREM*

302 which was implicated in IL-2 suppression [48]. These genes could potentially identify pan T
303 cell dysfunction markers within the GBM iTME [49].
304
305 *Interrogation of cell-cell interactions revealed critical role of SPP1-mediated crosstalk be-*
306 *tween MG and lymphocytes in the tumor periphery*
307 We finally investigated cell-cell interactions based on ligand-receptor expression levels
308 using the CellChat platform [50]. Considering that MG and lymphocytes displayed an impaired
309 activation signature in the tumor periphery, we focused our analysis on the tumor-peripheral
310 crosstalk between these cells (Figure 7A). This revealed SPP1 (Osteopontin) as a leading po-
311 tential cell-cell interaction mediator between MG and lymphocytes (Figure 7A and 7B). MG
312 SPP1-mediated signaling was as well among the most significant interactions, when investigat-
313 ing cell-cell communication across all cell types and both sites (Figure 7 – figure supplement
314 1A, 1B). Further, we found that *SPP1* is mainly expressed by MG rather than glioma cells,
315 contrary to previous reports [51] (Figure 7C, Figure 7 – figure supplement 1C, 1D). MG SPP1
316 conveys different interactions, depending on the recipient cell binding receptor expression pro-
317 file. The predicted interactions of MG SPP1 with NK cells could be mediated via the integrin
318 complex *ITGA4-ITGB1* (CD49d-CD29) (Figure 7A, 7C), whereas $CD4^+$ and $CD8^+$ T cells ex-
319 hibited strong interactions with MG via SPP1/CD44 interaction (Figure 7A, 7B). The
320 SPP1/CD44 axis was recently described to suppress T cell activation and proliferation [52].
321 The identified MG SPP1-mediated interactions might represent potential targets to modulate
322 MG-lymphocyte crosstalk in the tumor periphery.

323 **Discussion**

324 In this study, we combined single-cell RNA sequencing and flow cytometry to interro-
325 gate the regional leukocyte activation signature in patient-matched biopsies from contrast-en-
326 hancing tumor center, infiltrative peripheral rim, and blood PBMCs of grade 4 glioma patients.
327 Our analyses revealed a distinct, regionally dependent transcriptional profile for most of the
328 investigated cell populations. While peripheral MG and cytotoxic cells predominantly dis-
329 played an impaired activation signature, MdMs showed pro-inflammatory traits in the tumor
330 periphery, however, were less abundant there compared to the tumor center, which was reported
331 by others as well [12, 13]. Supplemented with transcriptional analysis of paired PBMC samples,
332 we provide an in-depth characterization of the three main immunological compartments of
333 grade 4 glioma.

334 Previous studies focused on the description of the TME of grade 4 glioma, which also
335 considered regional differences, yet they focused primarily at neoplastic cells rather than the
336 immune compartment [12]. Others investigated the differences in the iTME composition be-
337 tween primary and metastatic brain tumors [5, 6]. Interestingly, the two latter ones reported
338 differences in the iTME composition between *IDH1*^{wt} and *IDH1*^{mut} glioma. Of note, both au-
339 thors included low-grade and even pre-treated recurrent glioma patients into the *IDH1*^{mut} group,
340 representing a quite heterogenous patient cohort. In this study, we aimed at providing a repre-
341 sentative selection of primary, treatment-naïve grade 4 glioma patients including *IDH1*^{wt} and
342 *IDH1*^{mut} to identify common transcriptional differences within the iTME between tumor center,
343 periphery and PBMC of grade 4 glioma. How far these regional differences vary between
344 *IDH1*^{wt} and *IDH1*^{mut} grade 4 glioma merits further investigation.

345 We identified a transcriptionally distinct MG subcluster, MG_1, which was enriched in
346 the infiltrative tumor periphery and displayed an anti-inflammatory/non-reactive phenotype. A
347 similar MG subpopulation expressing a comparable gene signature was recently described to
348 be enriched in Alzheimer's disease patients [53].

349 Additionally, the peripheral cytotoxic cell compartment exhibited an impaired activa-
350 tion state, including a downregulated IFN response signature in CD8^{+} T cells. Induction of an
351 IFN response state was described as a consequence of T cell receptor-mediated IFN-γ produc-
352 tion, likely serving as an autocrine response and inducing the proliferative program [34]. Hence,
353 the reduced autocrine IFN-responsive state in the tumor peripheral CD8^{+} T cells, together with
354 downregulated proliferative and co-stimulatory genes emphasized their impaired activation in
355 the peripheral infiltration zone. Recently, we showed that the response to immunotherapy in
356 GBM is indeed region dependent. For this, we cultured GBM explants in perfusion bioreactors

357 and treated with anti-CD47, anti-PD1, or their combination which induced an IFN-γ response
358 only in the tumor center, but not periphery [54]. Adding experimental support to the here de-
359 scribed impaired activation signature in the tumor periphery.

360 By exploring the transcriptional trajectory of $CD8^+$ T cells from the blood circulation
361 into the immunosuppressive TME of the tumor periphery, we uncovered $CX3CR1^{high}$ and
362 $CX3CR1^{int}$ effector and memory $CD8^+$ T cells, respectively, to be highly enriched in the PBMC,
363 but absent in the iTME. Recently, adoptive transfer studies of $CX3CR1^+$ $CD8^+$ T cells in a mel-
364 anoma mouse model significantly suppressed tumor growth [41]. Others identified increased
365 frequencies of $CX3CR1^+$ $CD8^+$ T cells in non-small cell lung and melanoma patients who re-
366 sponded to anti-PD-1 therapy, where these cells exhibited migratory capabilities into the tumor
367 site followed by potent tumor rejection [40, 41]. Thus, the authors proposed T cell CX3CR1
368 expression as a predictor of response to ICI therapy. Even though $CX3CR1^+$ $CD8^+$ T cells might
369 not be specific to GBM, as they are found in healthy donor and different inflammation related
370 conditions [38-41], the absence of these effector and potentially ICI therapy responsive $CD8^+$
371 T cells in the glioma TME could serve as an additional explanation for the disappointing out-
372 come of clinical trials using ICI in glioma patients.

373 The observed T_{rm} exhaustion phenotype of the glioma residing $CD8^+$ T cells was re-
374 cently reported as well for tumor-infiltrating $PD\text{-}1^{high}$ $CD8^+$ T cells in hepatocellular carcinoma
375 [44]. Whether these glioma-associated $CD8^+$ T cells really possess tumor-specificity requires
376 further study. Particularly in the light of a recent study by Smolders and colleagues who re-
377 ported a consistent brain-resident $CD8^+$ T cell population in a miscellaneous autopsy cohort of
378 patients with neurological disorders excluding brain malignancies (Alzheimer's disease, Par-
379 kinson's disease, dementia, depression, multiple sclerosis), as well as patients with no known
380 brain disease. These brain-resident $CD8^+$ T cells displayed a remarkably consistent T_{rm} pheno-
381 type [55]. The authors further showed high expression of inhibitory receptors CTLA-4 and PD-
382 1 on the brain-resident $CD8^+$ T_{rm} cells, which is in line with the core phenotypic signature of
383 T_{rm} cells from other tissues [56, 57]. Yet, the brain $CD8^+$ T_{rm} cells showed a preserved inflam-
384 matory potential with substantial production of IFN-γ and TNF-α upon *ex vivo* stimulation.
385 They concluded that extensive immune activation with release of highly neurotoxic lytic en-
386 zymes, such as perforin and granzyme B, harmfully impacts the brain parenchyma and should
387 be tightly controlled, whilst maintaining the capability to elicit a fast inflammatory response
388 when a neurotropic virus threatens the CNS [55]. Therefore, inhibitory receptors like PD-1 and
389 CTLA-4 on brain $CD8^+$ T_{rm} cells may support CNS homeostasis by preventing uncontrolled T
390 cell reactivity, and the availability of the receptor ligands may determine their inhibitory effect.

While this may represent a well-balanced equilibrium under healthy conditions, the tumor setting leads to its disruption with upregulation of inhibitory ligands like PD-L1 on glioma cells and CD86 on GAMs, leading to the dysfunctional state seen in the glioma-residing $CD8^+$ T_{rm} cells.

Another study comprehensively showed, that peripheral infections generate antigen-specific $CD8^+$ T_{rm} cells in the brain, mediating protection against CNS infections [42]. These data could implicate that the glioma-associated $CD8^+$ T cells are devoid of tumor-specific reactivity, but rather represent a pre-existing T cell population generated after peripheral infections, which acquired a dysfunctional state upon glioma formation. To test this hypothesis, further characterization of these cells is required, including analysis of T cell receptor clonality and tumor-specificity by patient-matched T cell/glioma-sphere co-culture assays.

Lastly, our cell-cell interaction analysis revealed signaling pathways between peripheral MG and lymphocytes potentially inducing the observed impaired activation signature. The predicted interaction between MG SPP1 and NK cells integrin complex *ITGA4-ITGB1* (CD49d-CD29), might mediate NK cell adhesion and migration [58]. This may facilitate interaction of inhibitory NK receptors KLRB1 and CD94/NKG2A with MG C-type lectin-related ligands and HLA-E, respectively, which could explain the observed impaired activation state of peripheral NK cells. Moreover, SPP1/CD44 interaction in T lymphocytes was described to suppress cell activation and proliferation [52]. In a comprehensive approach where transcriptional states of human MG were mapped during aging and disease, *SPP1* was found to be differentially expressed in aging-microglia. This was associated to a doubling of the abundance of $SPP1^+$ GAMs in GBM samples compared to MG from age-matched controls [59]. These observations support a possible role of MG SPP1 in glioma progression. More recently, myeloid-derived osteopontin (encoded by *SPP1*) was shown to trigger a chronic activation of NFAT2 in tumor-reactive $CD8^+$ T cells, leading to T cell dysfunction and exhaustion in an experimental mouse model of GBM [60]. This adds an additional layer of mechanistic evidence for the *SPP1*/Osteopontin-mediated signaling axis leading to $CD8^+$ T cell dysfunction in GBM.

Limitations of our study include the limited patient number, thereby our study was neither designed nor powered to explore differences in neoplastic cells, given the high inter- and intra-patient variability in glioma cells [12]. Importantly, our dataset establishes a starting point for further interrogation and provides a first analysis of the transcriptional landscape of the major immune populations in grade 4 glioma within three important regional compartments. Further, we confirmed the observed phenotype of $CD8^+$ T cells in the blood and tumor periphery by flow cytometry in a cohort of ten additional patients, addressing possible generalization

425 concerns. Together, we provide a regionally resolved map of leukocyte activation in the TME
426 and blood circulation from grade 4 glioma patients, helping the research community to uncover
427 novel therapeutic strategies to combat this fatal disease.

428 **Methods**

Key Resources Table				
Reagent type (species) or resource	**Designation**	**Source or reference**	**Identifiers**	**Additional information**
biological sample (Human adult GBM tissue samples)	Tumor Center; Tumor Periphery	Neurosurgical Clinic of the University Hospital of Basel, Switzerland		
biological sample (Human Peripheral Blood Buffy Coat)	PBMC	Neurosurgical Clinic of the University Hospital of Basel, Switzerland		
antibody	Rat monoclonal anti-human/mouse CD11b (clone M1/70), FITC	BioLegend	Cat# 101206	FACS: 1:50
antibody	Mouse monoclonal anti-human CD45 (clone 2D1), FITC	BioLegend	Cat# 368508	FACS: 1:50
antibody	Fc-Block anti-human CD16/CD32, TruStain FcX	BioLegend	Cat# 422302	FACS: 1:50
antibody	Mouse monoclonal anti-human CD45RO (clone UCHL1), APC	BioLegend	Cat# 304210	FACS: 1:25
antibody	Mouse monoclonal anti-human CD45RA (clone HI100), PE	BioLegend	Cat# 304108	FACS: 1:25
antibody	Mouse monoclonal anti-human CD3e (clone UCHT1), BV650	BioLegend	Cat# 300468	FACS: 1:25
antibody	Mouse monoclonal anti-human CD8a (clone RPA-T8), BV421	BioLegend	Cat# 301036	FACS: 1:25

antibody	Mouse monoclonal anti-human CCR7 (clone G043H7), FITC	BioLegend	Cat# 353216	FACS: 1:25
antibody	Mouse monoclonal anti-human CD62L (clone DREG-56), AF700	BioLegend	Cat# 304820	FACS: 1:50
antibody	Mouse monoclonal anti-human CD69 (clone FN50), APC/Cy7	BioLegend	Cat# 310914	FACS: 1:25
antibody	Mouse monoclonal anti-human CD103 (clone Ber-ACT8), PerCP/Cy5.5	BioLegend	Cat# 350226	FACS: 1:25
antibody	Rat monoclonal anti-human CX3CR1 (clone 2A9-1), PE-Cy7	BioLegend	Cat# 341612	FACS: 1:25
commercial assay or kit	Chromium Single Cell 3' Reagent Kits v3	10x Genomics	Cat# CG000183	
commercial assay or kit	BioAnalyzer High Sensitivity DNA Analysis kit	Agilent	Cat# 5067-4626	
commercial assay or kit	Qubit dsDNA High Sensitiivity assay kit	ThermoFisher	Cat# Q33230	
chemical compound, drug	Collagenase-4	Worthington Biochemical Cooperation	Cat# LS004188	
chemical compound, drug	DNAse1	Roche	Cat# 10104159001	
chemical compound, drug	ACK lysis buffer	Gibco	Cat# A1049201	

chemical compound, drug	Bambanker	Nippon Genetics	Cat# BB01	
chemical compound, drug	Sucorse	Sigma Aldrich	Cat# 84100	
chemical compound, drug	Ficoll-Paque PLUS	Cytiva	Cat# 17144002	
chemical compound, drug	Live/Dead Fixable Near IR Dead Stain Kit, APC-Cy7	ThermoFisher	Cat# L34976	
chemical compound, drug	Zombie Aqua Fixable Viability Kit	BioLegend	Cat# 423102	
software, algorithm	R environment, version 4.1	R Core Team	https://www.r-project.org/	
software, algorithm	GraphPad Prism 9	GraphPad Software Inc.	N/A	
software, algorithm	Flow Jo, version 10.8.1	Tree Star	N/A	

Ethics statement

Human adult GBM tissue samples were obtained at the Neurosurgical Clinic of the University Hospital of Basel, Switzerland in accordance with the Swiss Human Research Act and institutional ethics commission (EKNZ 02019-02358). All patients gave written informed consent for tumor biopsy collection and signed a declaration permitting the use of their biopsy specimens in scientific research, including storage in our brain tumor biobank (Req-2019-00553). All patient identifying information was removed and tissue was coded for identification.

Glioma tissue dissociation

440 Resected glioma tissue samples were immediately placed on ice and transferred to the
441 laboratory for single cell dissociation within 2-3 h after resection. Human brain tissue was man-
442 ually minced using razor blades and enzymatically dissociated at 37°C for 30 minutes with 1
443 mg/ml collagenase-4 (#LS004188, Worthington Biochemical Corporation, USA) and 250 U/ml
444 DNAse1 (#10104159001, Roche, Switzerland) in a buffer containing Hank's Balanced Salt
445 Solution (HBSS) with Ca^{2+}/Mg^{2+}, 1% MEM non-essential amino acids (Gibco, USA), 1 mM
446 sodium pyruvate (Gibco), 44 mM sodium bi-carbonate (Gibco), 25 mM HEPES (Gibco), 1%
447 GlutaMAX (Gibco) and 1% antibiotic-antimycotic (Sigma-Aldrich, USA). Cells were filtered
448 and separated from dead cells, debris and myelin by a 0.9 M sucrose (#84100, Sigma Aldrich)
449 density gradient centrifugation. Upon ACK-lysis for removal of erythrocytes (#A1049201,
450 Gibco) the now generated single-cell suspension (SCS) was washed, counted and frozen in
451 Bambanker (#BB01, Nippon Genetics, Germany) in liquid nitrogen until use.
452
453 *PBMCs (Peripheral blood mononuclear cells) preparation*
454 Patient blood samples were directly placed on ice and transferred to the laboratory for
455 PBMC isolation. Blood samples were centrifuged to separate buffy coat from plasma and eryth-
456 rocytes, followed by standard density gradient centrifugation protocol (#17144002, Ficoll-
457 Paque PLUS, Cytiva, USA) to isolate PBMCs. PBMCs were frozen in Bambanker (#BB01,
458 Nippon Genetics, Germany) in liquid nitrogen until use.
459
460 *FACS sorting for single cell RNA sequencing (scRNA-seq)*
461 Cryopreserved tumor digests from glioma samples (center and periphery), as well as
462 autologous PBMCs were thawed and washed with excess ice-cold 1xPBS and spun down at
463 350xg for 5 min. Subsequently, the cells were stained with Live/Dead (APC-Cy7 (Near IR), #
464 L34976, Thermo Fischer) and a cocktail of fluorescently-conjugated antibodies CD11b (FITC,
465 clone M1/70, #101206, BioLegend) and CD45 (FITC, clone 2D1, #368508, BioLegend), and
466 large debris were removed with a 40-µm strainer. All samples were acquired on the BD FACS
467 ARIA Fusion III (Becton Dickinson GmbH, Germany). For single-cell RNA-seq experiments,
468 live and single gated cells were sorted into non-immune cell ($CD45^{-}CD11b^{-}$) and immune cell
469 ($CD45^{+}CD11b^{+}$) populations. Both populations were directly sorted into Eppendorf tubes with
470 1xPBS supplemented with 1% BSA for single cell RNA sequencing.
471
472 *Single cell RNA sequencing (scRNA-seq) – Library preparation and sequencing*

473 Single-cell RNA-seq was performed using Chromium Single Cell 3' GEM, Library &
474 Gel Bead Kit v3 (#CG000183, 10x Genomics, Pleasanton, CA, USA) following the manufac-
475 turer's protocol. Briefly, non-immune cells and immune cells were mixed at a defined ratio of
476 1:4. Roughly 8000-10000 cells per sample, diluted at a density of 100–800 cells/µL in PBS plus
477 1% BSA determined by Cellometer Auto 2000 Cell Viability Counter (Nexelom Bioscience,
478 Lawrence, MA USA), and were loaded onto the chip. The quality and concentration of both
479 cDNA and libraries were assessed using an Agilent BioAnalyzer with High Sensitivity kit
480 (#5067-4626, Agilent, Santa Clara, CA USA) and Qubit Fluorometer with dsDNA HS assay
481 kit (#Q33230, Thermo Fischer Scientific, Waltham, MA USA) according to the manufacturer's
482 recommendation. For sequencing, samples were mixed in equimolar fashion and sequenced on
483 an Illumina HiSeq 4000 with a targeted read depth of 50,000 reads/cell and sequencing param-
484 eters were set for Read1 (28 cycles), Index1 (8 cycles), and Read2 (91 cycles).
485
486 *Single cell RNA sequencing (scRNA-seq) - Computational analysis*
487 The dataset was analyzed by the Bioinformatics Core Facility, Department of Biomed-
488 icine, University of Basel. Read quality was controlled with the FastQC tool (version 0.11.5).
489 Sequencing files were processed using the Salmon Alevin tool (v 1.3.0) [61] to perform quality
490 control, sample demultiplexing, cell barcode processing, pseudo-alignment of cDNA reads to
491 the human Gencode v35 reference and counting of UMIs. Parameters *--keepCBFraction 1* and
492 *--maxNumBarcodes 100000* were used.
493 Processing of the UMI counts matrix was performed using the Bioconductor packages
494 DropletUtils (version 1.8.0) [62, 63], scran (version 1.16.0) [64, 65] and scater (version 1.16.2)
495 [66], following mostly the steps illustrated in the OSCA book (http://bioconduc-
496 tor.org/books/release/OSCA/) [65, 67]. Filtering for high-quality cells was done based on li-
497 brary size (at least 2,000 UMI counts per cell), the number of detected genes (at least 700 genes
498 detected) and the percentage of reads mapping to mitochondrial genes (larger than 0% and
499 lower than 15%), based on the distribution observed across cells. Low-abundance genes with
500 average counts per cell lower than 0.006 were filtered out. The presence of doublet cells was
501 investigated with the scDblFinder package (version 1.2.0), and suspicious cells were filtered
502 out (score > 0.6). After quality filtering, the resulting dataset consisted of UMI counts for
503 15,523 genes and 45,466 cells, ranging from 803 to 9,121 per sample.
504 UMI counts were normalized with size factors estimated from pools of cells created
505 with the scran package *quickCluster()* function [64, 68]. To distinguish between genuine bio-
506 logical variability and technical noise we modeled the variance of the log-expression across

genes using a Poisson-based mean-variance trend. The scran package *denoisePCA()* function was used to denoise log-expression data by removing principal components corresponding to technical noise. Consistent to the *findElbowPoint()* function from the PCAtools Bioconductor package, this led us to retain the top 5 principal components (PCs), explaining 48.3% of the total variance in the dataset, for the clustering and dimensionality reduction steps.

Since the excluded deeper PCs (PC8 and 10) were associated to patient-specific effects (which in our experimental setup are also confounded with batch effects), this choice dispensed us from performing an additional correction for patient-specific effects. A quantitative test of overlap of cells across patients was made using the CellMixS package [69] (version 1.12.0) developed to quantify the effectiveness of batch correction methods. We used the cell-specific mixing (CMS) score, which highlighted a very good overlap across cells from different patients in the lymphoid compartment and for the monocytes. The myeloid compartment displayed a slightly elevated patient-specific structure, while it was most pronounced for the CD45 negative subset.

A t-stochastic neighbor embedding (t-SNE) was built with a perplexity of 50 using the top most variable genes (141 genes with estimated biological variance > 0.3, excluding genes with highest proportion of reads in the ambient RNA pool estimated from empty droplets), and the denoised principal components as input. Clustering of cells was performed with hierarchical clustering on the Euclidean distances between cells (with Ward's criterion to minimize the total variance within each cluster [70]; package cluster version 2.1.0). The number of clusters used for following analyses was identified by applying a dynamic tree cut (package dynamicTreeCut, version 1.63-1) [71], resulting in 10 with argument *deepSplit* set to 1, or 22 clusters with argument *deepSplit* set to 2. This clustering was validated with an alternative clustering approach using a graph-based approach and Louvain algorithm for community detection (using the *FindNeighbors()* and *FindClusters()* functions from the *Seurat* package [72] (version 4.3.0), with a resolution of 0.7) which showed a good correspondence to our hierarchical clustering.

The *findMarkers* function of the scran package was used to find the best markers across annotated cell types (parameters *direction="up"* and *pval.type="any"*). The top 10 markers for each cell type were extracted and pooled to from a list of 68 markers.

The Bioconductor package *SingleR* (version 1.2.4) was used for cell-type annotation of the cells [73] using as references (i) a public bulk RNA-seq dataset of sorted immune cell types from human PBMC samples [16], available through the *celldex* Bioconductor package; (ii) a bulk RNA-seq dataset of sorted immune cell types from the tumor microenvironment of human gliomas [5] (UMI count matrix and annotation downloaded from

541 https://joycelab.shinyapps.io/braintime/); (iii) a 10X genomics scRNA-seq dataset of TAMs
542 from the tumor micro-environment of glioblastoma tumors from 7 newly diagnosed human
543 patients [9]; (iv) a microglia and a macrophage signature scores were defined by averaging the
544 center and scaled expression levels of gene lists obtained in [7] and (v) a Smartseq2 scRNA-
545 seq dataset of IDH-wild-type glioblastoma tumors [17] (downloaded from GEO accession
546 GSE131928). An endothelial score was defined by averaging the center and scaled expression
547 levels of the genes *CDH5*, *VWF*, *CD34* and *PECAM1*.

548 The SingleR high-quality assignments (pruned scores) from the comparisons to the mul-
549 tiple references (some being better at enlightening some immune subsets than others) were used
550 to manually derive a consensus cell type annotation for each cluster. This manual annotation
551 was done jointly with the input from the signature scores and relative expression patterns of
552 known marker genes and of cluster-specific genes.

553 When we judged that the resolution was not sufficient to discriminate well the subtypes
554 of cells within a subset (in particular for the CD45neg and myeloid cells subsets), we isolated
555 these cells and re-performed selection of hyper-variable genes, dimensionality reduction and
556 clustering on the isolated subset.

557 Differential abundance analysis of the identified cell types between tumor sites was
558 performed using *limma-voom* [74]. This method, implemented in the *diffcyt* package, was
559 shown to be able to handle well the overdispersion in the cell type proportions estimates typi-
560 cally observed with single cell technologies [75]. Differential abundance of cell types was con-
561 sidered to be significant at a false discovery rate (FDR) lower than 5 %. To provide increased
562 resolution into local trends within the tumor innate immune subset we used the *miloR* biocon-
563 ductor package [76] (version 1.4.0) to test for differential abundance on neighborhoods of a *k*-
564 nearest neighbor graph. Testing was done with *limma-voom* similarly to above. Cell type labels
565 were assigned to each neighborhood by finding the most abundant cell type across cells and
566 requiring that at least 70% of the cells come from one cell type.

567 Differential expression between tumor sites, or between PBMC cells and tumor periph-
568 ery cells, stratified by annotated cell type, was performed using a pseudo-bulk approach, which
569 was shown to be the best-performing approach for differential expression testing in recent
570 benchmarks [77]. UMI counts were summed across cells from each cell type in each sample
571 when at least 20 cells could be aggregated. The aggregated samples were then treated as bulk
572 RNA-seq samples [78] and for each pairwise comparison genes were filtered to keep genes
573 detected in at least 5% of the cells aggregated. The package edgeR (version 3.30.3) [79] was
574 used to perform TMM normalization [80] and to test for differential expression with the

575 Generalized Linear Model (GLM) framework, using a model accounting for patient-specific
576 effects. Genes with a FDR lower than 5 % were considered differentially expressed. To validate
577 our differential expression analysis, we rerun a pseudo-bulk expression analysis using DESeq2
578 (version 1.38.3) [81] for the main immune populations in the periphery versus center and pe-
579 riphery versus PBMC comparison. Although, the results were not identical, they overall agreed
580 with edgeR (Supplementary File 7). Gene set enrichment analysis was performed with the func-
581 tion camera [82] on gene sets from the Molecular Signature Database (MSigDB, version 7.4)
582 [27, 83]. We retained only sets containing more than 5 genes, and gene sets with a FDR lower
583 than 5% were considered as significant.
584
585 *Cell chat analysis*
586 The R package CellChat (1.1.3) [50] was used to analyze cell-cell interactions in our
587 dataset (with previously annotated 9 cell types). We followed the recommended workflow to
588 infer the cell state-specific communications (using *identifyOverExpressedGenes*, *identifyOver-*
589 *ExpressedInteractions* and *projectData* with the default parameters). We performed 3 separate
590 analyses, on the center and the periphery subsets and a comparison analysis as described in the
591 official workflow. We visualized the significant interactions for the microglia cluster using
592 *netVisual_chord_gene* and used *plotGeneExpression* to display of the expression of all genes
593 involved SPP1 signaling pathway in the cell populations. Finally, *netAnalysis_signalin-*
594 *gRole_scatter* was used to calculate and visualize incoming and outgoing signaling strength.
595
596 *Flow cytometry analysis of paired PBMC and periphery samples*
597 Cryopreserved samples were thawed and washed with excess ice-cold 1xPBS and spun
598 down at 350xg for 5 min. Cells were resuspended in FACS buffer (PBS plus 2% FBS) and
599 blocked with monoclonal antibody to CD16/32 (Human TruStain FcX, #422302, Biolegend)
600 for 10 min at 4°C before staining with surface antibodies: CD45RA (PE, clone HI100,
601 #304108), CD45RO (APC, clone UCHL1, #304210), CD3e (BV650, clone UCHT1, #300468),
602 CD8a (BV421, clone RPA-T8, #301036), CCR7 (FITC, clone G043H7, #353216), CD62L
603 (AF700, clone DREG-56, #304820), CD69 (APC-Cy7, clone FN50, #310914), CD103
604 (PerCP/Cy5.5, clone Ber-ACT8, #350226) and CX3CR1 (PE/Cy7, clone 2A9-1, #341612). All
605 antibodies were purchased from BioLegend, USA. Cells were stained for 30 min at 4°C, and
606 subsequently washed with FACS buffer. To exclude dead cells Zombie Aqua Fixable Viability
607 Kit (#423102, 1:100, BioLegend) was added. Acquisition was performed on a CytoFLEX

(Beckman). Data was analyzed using FlowJo software, version 10.8.1 (TreeStar). Gates were drawn by using Fluorescent Minus One (FMO) controls.

Statistical analysis of flow cytometry data

Data analysis and graph generation was performed using GraphPad Prism 9 (GraphPad Prism Software Inc.). Paired comparisons between two groups were performed using Wilcoxon matched-pairs signed rank test. Differences of more than two paired groups were assessed using repeated measures one-way ANOVA test, followed by post-hoc Šidák's multiple comparisons correction. A p value < 0.05 was considered statistically significant. $*p \leq 0.05$, $**p \leq 0.01$, $***p \leq 0.001$, $****p \leq 0.0001$.

Graphical illustrations

All graphical illustrations were created with BioRender.com.

622 **Data availability**

623 The UMI count matrix and cell metadata from the scRNA-seq dataset are available on
624 GEO under accession number GSE197543. The remaining data are available within the Article
625 and Supplementary Information.

References

1. Stupp, R., W.P. Mason, M.J. van den Bent, M. Weller, B. Fisher, M.J. Taphoorn, K. Belanger, A.A. Brandes, C. Marosi, U. Bogdahn, J. Curschmann, R.C. Janzer, S.K. Ludwin, T. Gorlia, A. Allgeier, D. Lacombe, J.G. Cairncross, E. Eisenhauer, and R.O. Mirimanoff, *Radiotherapy plus concomitant and adjuvant temozolomide for glioblastoma.* N Engl J Med, 2005. **352**(10): p. 987-96.

2. Bowman, R.L., F. Klemm, L. Akkari, S.M. Pyonteck, L. Sevenich, D.F. Quail, S. Dhara, K. Simpson, E.E. Gardner, C.A. Iacobuzio-Donahue, C.W. Brennan, V. Tabar, P.H. Gutin, and J.A. Joyce, *Macrophage Ontogeny Underlies Differences in Tumor-Specific Education in Brain Malignancies.* Cell Rep, 2016. **17**(9): p. 2445-2459.

3. Reardon, D.A., T.J. Kaley, J. Dietrich, J.L. Clarke, G.P. Dunn, M. Lim, T.F. Cloughesy, H.K. Gan, A.J. Park, P. Schwarzenberger, T. Ricciardi, M.J. Macri, A. Ryan, and R.R. Venhaus, *Phase 2 study to evaluate safety and efficacy of MEDI4736 (durvalumab [DUR]) in glioblastoma (GBM) patients: An update.* Journal of Clinical Oncology, 2017. **35**(15_suppl): p. 2042-2042.

4. Reardon, D.A., A. Omuro, A.A. Brandes, J. Rieger, A. Wick, J. Sepulveda, S. Phuphanich, P. de Souza, M.S. Ahluwalia, M. Lim, G. Vlahovic, and J. Sampson, *OS10.3 Randomized Phase 3 Study Evaluating the Efficacy and Safety of Nivolumab vs Bevacizumab in Patients With Recurrent Glioblastoma: CheckMate 143.* Neuro-Oncology, 2017. **19**(Suppl 3): p. iii21-iii21.

5. Klemm, F., R.R. Maas, R.L. Bowman, M. Kornete, K. Soukup, S. Nassiri, J.P. Brouland, C.A. Iacobuzio-Donahue, C. Brennan, V. Tabar, P.H. Gutin, R.T. Daniel, M.E. Hegi, and J.A. Joyce, *Interrogation of the Microenvironmental Landscape in Brain Tumors Reveals Disease-Specific Alterations of Immune Cells.* Cell, 2020. **181**(7): p. 1643-1660.e17.

6. Friebel, E., K. Kapolou, S. Unger, N.G. Núñez, S. Utz, E.J. Rushing, L. Regli, M. Weller, M. Greter, S. Tugues, M.C. Neidert, and B. Becher, *Single-Cell Mapping of Human Brain Cancer Reveals Tumor-Specific Instruction of Tissue-Invading Leukocytes.* Cell, 2020. **181**(7): p. 1626-1642.e20.

7. Müller, S., G. Kohanbash, S.J. Liu, B. Alvarado, D. Carrera, A. Bhaduri, P.B. Watchmaker, G. Yagnik, E. Di Lullo, M. Malatesta, N.M. Amankulor, A.R. Kriegstein, D.A. Lim, M. Aghi, H. Okada, and A. Diaz, *Single-cell profiling of human gliomas reveals macrophage ontogeny as a basis for regional differences in macrophage activation in the tumor microenvironment.* Genome Biology, 2017. **18**(1): p. 234.

8. Abdelfattah, N., P. Kumar, C. Wang, J.-S. Leu, W.F. Flynn, R. Gao, D.S. Baskin, K. Pichumani, O.B. Ijare, S.L. Wood, S.Z. Powell, D.L. Haviland, B.C. Parker Kerrigan, F.F. Lang, S.S. Prabhu, K.M. Huntoon, W. Jiang, B.Y.S. Kim, J. George, and K. Yun, *Single-cell analysis of human glioma and immune cells identifies S100A4 as an immunotherapy target.* Nature Communications, 2022. **13**(1): p. 767.

9. Pombo Antunes, A.R., I. Scheyltjens, F. Lodi, J. Messiaen, A. Antoranz, J. Duerinck, D. Kancheva, L. Martens, K. De Vlaminck, H. Van Hove, S.S. Kjølner Hansen, F.M. Bosisio, K. Van der Borght, S. De Vleeschouwer, R. Sciot, L. Bouwens, M. Verfaillie, N. Vandamme, R.E. Vandenbroucke, O. De Wever, Y. Saeys, M. Guilliams, C. Gysemans, B. Neyns, F. De Smet, D. Lambrechts, J.A. Van Ginderachter, and K.

Movahedi, *Single-cell profiling of myeloid cells in glioblastoma across species and disease stage reveals macrophage competition and specialization.* Nature Neuroscience, 2021. **24**(4): p. 595-610.

10. Goswami, S., T. Walle, A.E. Cornish, S. Basu, S. Anandhan, I. Fernandez, L. Vence, J. Blando, H. Zhao, S.S. Yadav, M. Ott, L.Y. Kong, A.B. Heimberger, J. de Groot, B. Sepesi, M. Overman, S. Kopetz, J.P. Allison, D. Pe'er, and P. Sharma, *Immune profiling of human tumors identifies CD73 as a combinatorial target in glioblastoma.* Nature Medicine, 2020. **26**(1): p. 39-46.

11. Chen, A.X., R.D. Gartrell, J. Zhao, P.S. Upadhyayula, W. Zhao, J. Yuan, H.E. Minns, A. Dovas, J.N. Bruce, A. Lasorella, A. Iavarone, P. Canoll, P.A. Sims, and R. Rabadan, *Single-cell characterization of macrophages in glioblastoma reveals MARCO as a mesenchymal pro-tumor marker.* Genome Medicine, 2021. **13**(1): p. 88.

12. Darmanis, S., S.A. Sloan, D. Croote, M. Mignardi, S. Chernikova, P. Samghababi, Y. Zhang, N. Neff, M. Kowarsky, C. Caneda, G. Li, S.D. Chang, I.D. Connolly, Y. Li, B.A. Barres, M.H. Gephart, and S.R. Quake, *Single-Cell RNA-Seq Analysis of Infiltrating Neoplastic Cells at the Migrating Front of Human Glioblastoma.* Cell Rep, 2017. **21**(5): p. 1399-1410.

13. Landry, A.P., M. Balas, S. Alli, J. Spears, and Z. Zador, *Distinct regional ontogeny and activation of tumor associated macrophages in human glioblastoma.* Scientific Reports, 2020. **10**(1): p. 19542.

14. Louis, D.N., A. Perry, P. Wesseling, D.J. Brat, I.A. Cree, D. Figarella-Branger, C. Hawkins, H.K. Ng, S.M. Pfister, G. Reifenberger, R. Soffietti, A. von Deimling, and D.W. Ellison, *The 2021 WHO Classification of Tumors of the Central Nervous System: a summary.* Neuro-Oncology, 2021. **23**(8): p. 1231-1251.

15. Linderman, G.C., M. Rachh, J.G. Hoskins, S. Steinerberger, and Y. Kluger, *Fast interpolation-based t-SNE for improved visualization of single-cell RNA-seq data.* Nat Methods, 2019. **16**(3): p. 243-245.

16. Monaco, G., B. Lee, W. Xu, S. Mustafah, Y.Y. Hwang, C. Carré, N. Burdin, L. Visan, M. Ceccarelli, M. Poidinger, A. Zippelius, J. Pedro de Magalhães, and A. Larbi, *RNA-Seq Signatures Normalized by mRNA Abundance Allow Absolute Deconvolution of Human Immune Cell Types.* Cell Rep, 2019. **26**(6): p. 1627-1640.e7.

17. Neftel, C., J. Laffy, M.G. Filbin, T. Hara, M.E. Shore, G.J. Rahme, A.R. Richman, D. Silverbush, M.L. Shaw, C.M. Hebert, J. Dewitt, S. Gritsch, E.M. Perez, L.N. Gonzalez Castro, X. Lan, N. Druck, C. Rodman, D. Dionne, A. Kaplan, M.S. Bertalan, J. Small, K. Pelton, S. Becker, D. Bonal, Q.-D. Nguyen, R.L. Servis, J.M. Fung, R. Mylvaganam, L. Mayr, J. Gojo, C. Haberler, R. Geyeregger, T. Czech, I. Slavc, B.V. Nahed, W.T. Curry, B.S. Carter, H. Wakimoto, P.K. Brastianos, T.T. Batchelor, A. Stemmer-Rachamimov, M. Martinez-Lage, M.P. Frosch, I. Stamenkovic, N. Riggi, E. Rheinbay, M. Monje, O. Rozenblatt-Rosen, D.P. Cahill, A.P. Patel, T. Hunter, I.M. Verma, K.L. Ligon, D.N. Louis, A. Regev, B.E. Bernstein, I. Tirosh, and M.L. Suvà, *An Integrative Model of Cellular States, Plasticity, and Genetics for Glioblastoma.* Cell, 2019. **178**(4): p. 835-849.e21.

712 18. Pinton, L., E. Masetto, M. Vettore, S. Solito, S. Magri, M. D'Andolfi, P. Del Bianco, G.
713 Lollo, J.P. Benoit, H. Okada, A. Diaz, A. Della Puppa, and S. Mandruzzato, *The immune*
714 *suppressive microenvironment of human gliomas depends on the accumulation of bone*
715 *marrow-derived macrophages in the center of the lesion.* J Immunother Cancer, 2019.
716 **7**(1): p. 58.

717 19. Nguyen, A.T., K. Wang, G. Hu, X. Wang, Z. Miao, J.A. Azevedo, E. Suh, V.M. Van
718 Deerlin, D. Choi, K. Roeder, M. Li, and E.B. Lee, *APOE and TREM2 regulate amyloid-*
719 *responsive microglia in Alzheimer's disease.* Acta Neuropathol, 2020. **140**(4): p. 477-
720 493.

721 20. Soroceanu, L., R. Murase, C. Limbad, E. Singer, J. Allison, I. Adrados, R. Kawamura,
722 A. Pakdel, Y. Fukuyo, D. Nguyen, S. Khan, R. Arauz, G.L. Yount, D.H. Moore, P.Y.
723 Desprez, and S.D. McAllister, *Id-1 is a key transcriptional regulator of glioblastoma*
724 *aggressiveness and a novel therapeutic target.* Cancer Res, 2013. **73**(5): p. 1559-69.

725 21. Papaspyridonos, M., I. Matei, Y. Huang, M. do Rosario Andre, H. Brazier-Mitouart,
726 J.C. Waite, A.S. Chan, J. Kalter, I. Ramos, Q. Wu, C. Williams, J.D. Wolchok, P.B.
727 Chapman, H. Peinado, N. Anandasabapathy, A.J. Ocean, R.N. Kaplan, J.P. Greenfield,
728 J. Bromberg, D. Skokos, and D. Lyden, *Id1 suppresses anti-tumour immune responses*
729 *and promotes tumour progression by impairing myeloid cell maturation.* Nature
730 Communications, 2015. **6**(1): p. 6840.

731 22. Holtman, I.R., D. Skola, and C.K. Glass, *Transcriptional control of microglia*
732 *phenotypes in health and disease.* The Journal of Clinical Investigation, 2017. **127**(9):
733 p. 3220-3229.

734 23. Nomaru, H., K. Sakumi, A. Katogi, Y.N. Ohnishi, K. Kajitani, D. Tsuchimoto, E.J.
735 Nestler, and Y. Nakabeppu, *Fosb gene products contribute to excitotoxic microglial*
736 *activation by regulating the expression of complement C5a receptors in microglia.* Glia,
737 2014. **62**(8): p. 1284-98.

738 24. Sweet, D.R., N.T. Vasudevan, L. Fan, C.E. Booth, K.S. Keerthy, X. Liao, V.
739 Vinayachandran, Y. Takami, D. Tugal, N. Sharma, E.R. Chan, L. Zhang, Y. Qing, S.L.
740 Gerson, C. Fu, A. Wynshaw-Boris, P. Sangwung, L. Nayak, P. Holvoet, K. Matoba, Y.
741 Lu, G. Zhou, and M.K. Jain, *Myeloid Krüppel-like factor 2 is a critical regulator of*
742 *metabolic inflammation.* Nature Communications, 2020. **11**(1): p. 5872.

743 25. Salojin, K.V., I.B. Owusu, K.A. Millerchip, M. Potter, K.A. Platt, and T. Oravecz,
744 *Essential role of MAPK phosphatase-1 in the negative control of innate immune*
745 *responses.* J Immunol, 2006. **176**(3): p. 1899-907.

746 26. Lee, H., S. Cha, M.S. Lee, G.J. Cho, W.S. Choi, and K. Suk, *Role of antiproliferative B*
747 *cell translocation gene-1 as an apoptotic sensitizer in activation-induced cell death of*
748 *brain microglia.* J Immunol, 2003. **171**(11): p. 5802-11.

749 27. Liberzon, A., C. Birger, H. Thorvaldsdóttir, M. Ghandi, J.P. Mesirov, and P. Tamayo,
750 *The Molecular Signatures Database (MSigDB) hallmark gene set collection.* Cell
751 systems, 2015. **1**(6): p. 417-425.

752 28. Walker, D.G. and L.F. Lue, *Immune phenotypes of microglia in human*
753 *neurodegenerative disease: challenges to detecting microglial polarization in human*
754 *brains.* Alzheimers Res Ther, 2015. **7**(1): p. 56.

755 29. Hopperton, K.E., D. Mohammad, M.O. Trépanier, V. Giuliano, and R.P. Bazinet,
756 *Markers of microglia in post-mortem brain samples from patients with Alzheimer's*
757 *disease: a systematic review.* Molecular Psychiatry, 2018. **23**(2): p. 177-198.

758 30. Hammond, T.R., C. Dufort, L. Dissing-Olesen, S. Giera, A. Young, A. Wysoker, A.J.
759 Walker, F. Gergits, M. Segel, J. Nemesh, S.E. Marsh, A. Saunders, E. Macosko, F.
760 Ginhoux, J. Chen, R.J.M. Franklin, X. Piao, S.A. McCarroll, and B. Stevens, *Single-*
761 *Cell RNA Sequencing of Microglia throughout the Mouse Lifespan and in the Injured*
762 *Brain Reveals Complex Cell-State Changes.* Immunity, 2019. **50**(1): p. 253-271.e6.

763 31. McQuade, A., Y.J. Kang, J. Hasselmann, A. Jairaman, A. Sotelo, M. Coburn, S.K.
764 Shabestari, J.P. Chadarevian, G. Fote, C.H. Tu, E. Danhash, J. Silva, E. Martinez, C.
765 Cotman, G.A. Prieto, L.M. Thompson, J.S. Steffan, I. Smith, H. Davtyan, M. Cahalan,
766 H. Cho, and M. Blurton-Jones, *Gene expression and functional deficits underlie*
767 *TREM2-knockout microglia responses in human models of Alzheimer's disease.* Nature
768 Communications, 2020. **11**(1): p. 5370.

769 32. Rothe, T., N. Ipseiz, M. Faas, S. Lang, F. Perez-Branguli, D. Metzger, H. Ichinose, B.
770 Winner, G. Schett, and G. Krönke, *The Nuclear Receptor Nr4a1 Acts as a Microglia*
771 *Rheostat and Serves as a Therapeutic Target in Autoimmune-Driven Central Nervous*
772 *System Inflammation.* Journal of immunology (Baltimore, Md. : 1950), 2017. **198**(10):
773 p. 3878-3885.

774 33. Saijo, K., B. Winner, C.T. Carson, J.G. Collier, L. Boyer, M.G. Rosenfeld, F.H. Gage,
775 and C.K. Glass, *A Nurr1/CoREST pathway in microglia and astrocytes protects*
776 *dopaminergic neurons from inflammation-induced death.* Cell, 2009. **137**(1): p. 47-59.

777 34. Szabo, P.A., H.M. Levitin, M. Miron, M.E. Snyder, T. Senda, J. Yuan, Y.L. Cheng,
778 E.C. Bush, P. Dogra, P. Thapa, D.L. Farber, and P.A. Sims, *Single-cell transcriptomics*
779 *of human T cells reveals tissue and activation signatures in health and disease.* Nature
780 Communications, 2019. **10**(1): p. 4706.

781 35. Alegre, M.L., P.J. Noel, B.J. Eisfelder, E. Chuang, M.R. Clark, S.L. Reiner, and C.B.
782 Thompson, *Regulation of surface and intracellular expression of CTLA4 on mouse T*
783 *cells.* J Immunol, 1996. **157**(11): p. 4762-70.

784 36. Johnson, D.B., M.J. Nixon, Y. Wang, D.Y. Wang, E. Castellanos, M.V. Estrada, P.I.
785 Ericsson-Gonzalez, C.H. Cote, R. Salgado, V. Sanchez, P.T. Dean, S.R. Opalenik, D.M.
786 Schreeder, D.L. Rimm, J.Y. Kim, J. Bordeaux, S. Loi, L. Horn, M.E. Sanders, P.B.
787 Ferrell, Jr., Y. Xu, J.A. Sosman, R.S. Davis, and J.M. Balko, *Tumor-specific MHC-II*
788 *expression drives a unique pattern of resistance to immunotherapy via LAG-3/FCRL6*
789 *engagement.* JCI insight, 2018. **3**(24): p. e120360.

790 37. Sciumè, G., G. De Angelis, G. Benigni, A. Ponzetta, S. Morrone, A. Santoni, and G.
791 Bernardini, *CX3CR1 expression defines 2 KLRG1+ mouse NK-cell subsets with distinct*
792 *functional properties and positioning in the bone marrow.* Blood, 2011. **117**(17): p.
793 4467-4475.

794 38. Böttcher, J.P., M. Beyer, F. Meissner, Z. Abdullah, J. Sander, B. Höchst, S. Eickhoff,
795 J.C. Rieckmann, C. Russo, T. Bauer, T. Flecken, D. Giesen, D. Engel, S. Jung, D.H.
796 Busch, U. Protzer, R. Thimme, M. Mann, C. Kurts, J.L. Schultze, W. Kastenmüller, and

797 P.A. Knolle, *Functional classification of memory CD8+ T cells by CX3CR1 expression.*
798 Nature Communications, 2015. **6**(1): p. 8306.

799 39. Gerlach, C., E.A. Moseman, S.M. Loughhead, D. Alvarez, A.J. Zwijnenburg, L.
800 Waanders, R. Garg, J.C. de la Torre, and U.H. von Andrian, *The Chemokine Receptor*
801 *CX3CR1 Defines Three Antigen-Experienced CD8 T Cell Subsets with Distinct Roles*
802 *in Immune Surveillance and Homeostasis.* Immunity, 2016. **45**(6): p. 1270-1284.

803 40. Yamauchi, T., T. Hoki, T. Oba, V. Jain, H. Chen, K. Attwood, S. Battaglia, S. George,
804 G. Chatta, I. Puzanov, C. Morrison, K. Odunsi, B.H. Segal, G.K. Dy, M.S. Ernstoff, and
805 F. Ito, *T-cell CX3CR1 expression as a dynamic blood-based biomarker of response to*
806 *immune checkpoint inhibitors.* Nature Communications, 2021. **12**(1): p. 1402.

807 41. Yan, Y., S. Cao, X. Liu, S.M. Harrington, W.E. Bindeman, A.A. Adjei, J.S. Jang, J. Jen,
808 Y. Li, P. Chanana, A.S. Mansfield, S.S. Park, S.N. Markovic, R.S. Dronca, and H.
809 Dong, *CX3CR1 identifies PD-1 therapy-responsive CD8+ T cells that withstand*
810 *chemotherapy during cancer chemoimmunotherapy.* JCI Insight, 2018. **3**(8).

811 42. Urban, S.L., I.J. Jensen, Q. Shan, L.L. Pewe, H.-H. Xue, V.P. Badovinac, and J.T. Harty,
812 *Peripherally induced brain tissue–resident memory CD8+ T cells mediate protection*
813 *against CNS infection.* Nature Immunology, 2020. **21**(8): p. 938-949.

814 43. Mackay, L.K., M. Minnich, N.A. Kragten, Y. Liao, B. Nota, C. Seillet, A. Zaid, K. Man,
815 S. Preston, D. Freestone, A. Braun, E. Wynne-Jones, F.M. Behr, R. Stark, D.G. Pellicci,
816 D.I. Godfrey, G.T. Belz, M. Pellegrini, T. Gebhardt, M. Busslinger, W. Shi, F.R.
817 Carbone, R.A. van Lier, A. Kallies, and K.P. van Gisbergen, *Hobit and Blimp1 instruct*
818 *a universal transcriptional program of tissue residency in lymphocytes.* Science, 2016.
819 **352**(6284): p. 459-63.

820 44. Ma, J., B. Zheng, S. Goswami, L. Meng, D. Zhang, C. Cao, T. Li, F. Zhu, L. Ma, Z.
821 Zhang, S. Zhang, M. Duan, Q. Chen, Q. Gao, and X. Zhang, *PD1(Hi) CD8(+) T cells*
822 *correlate with exhausted signature and poor clinical outcome in hepatocellular*
823 *carcinoma.* Journal for immunotherapy of cancer, 2019. **7**(1): p. 331-331.

824 45. Liu, X., Y. Wang, H. Lu, J. Li, X. Yan, M. Xiao, J. Hao, A. Alekseev, H. Khong, T.
825 Chen, R. Huang, J. Wu, Q. Zhao, Q. Wu, S. Xu, X. Wang, W. Jin, S. Yu, Y. Wang, L.
826 Wei, A. Wang, B. Zhong, L. Ni, X. Liu, R. Nurieva, L. Ye, Q. Tian, X.-W. Bian, and
827 C. Dong, *Genome-wide analysis identifies NR4A1 as a key mediator of T cell*
828 *dysfunction.* Nature, 2019. **567**(7749): p. 525-529.

829 46. Dan, L., L. Liu, Y. Sun, J. Song, Q. Yin, G. Zhang, F. Qi, Z. Hu, Z. Yang, Z. Zhou, Y.
830 Hu, L. Zhang, J. Ji, X. Zhao, Y. Jin, M.A. McNutt, and Y. Yin, *The phosphatase PAC1*
831 *acts as a T cell suppressor and attenuates host antitumor immunity.* Nature
832 Immunology, 2020. **21**(3): p. 287-297.

833 47. Bignon, A., A. Régent, L. Klipfel, A. Desnoyer, P. de la Grange, V. Martinez, O.
834 Lortholary, A. Dalloul, L. Mouthon, and K. Balabanian, *DUSP4-mediated accelerated*
835 *T-cell senescence in idiopathic CD4 lymphopenia.* Blood, 2015. **125**(16): p. 2507-18.

836 48. Maine, C.J., J.R. Teijaro, K. Marquardt, and L.A. Sherman, *PTPN22 contributes to*
837 *exhaustion of T lymphocytes during chronic viral infection.* Proceedings of the National
838 Academy of Sciences, 2016. **113**(46): p. E7231-E7239.

49. Li, H., A.M. van der Leun, I. Yofe, Y. Lubling, D. Gelbard-Solodkin, A.C.J. van Akkooi, M. van den Braber, E.A. Rozeman, J.B.A.G. Haanen, C.U. Blank, H.M. Horlings, E. David, Y. Baran, A. Bercovich, A. Lifshitz, T.N. Schumacher, A. Tanay, and I. Amit, *Dysfunctional CD8 T Cells Form a Proliferative, Dynamically Regulated Compartment within Human Melanoma.* Cell, 2019. **176**(4): p. 775-789.e18.

50. Jin, S., C.F. Guerrero-Juarez, L. Zhang, I. Chang, R. Ramos, C.-H. Kuan, P. Myung, M.V. Plikus, and Q. Nie, *Inference and analysis of cell-cell communication using CellChat.* Nature Communications, 2021. **12**(1): p. 1088.

51. Wei, J., A. Marisetty, B. Schrand, K. Gabrusiewicz, Y. Hashimoto, M. Ott, Z. Grami, L.Y. Kong, X. Ling, H. Caruso, S. Zhou, Y.A. Wang, G.N. Fuller, J. Huse, E. Gilboa, N. Kang, X. Huang, R. Verhaak, S. Li, and A.B. Heimberger, *Osteopontin mediates glioblastoma-associated macrophage infiltration and is a potential therapeutic target.* J Clin Invest, 2019. **129**(1): p. 137-149.

52. Klement, J.D., A.V. Paschall, P.S. Redd, M.L. Ibrahim, C. Lu, D. Yang, E. Celis, S.I. Abrams, K. Ozato, and K. Liu, *An osteopontin/CD44 immune checkpoint controls CD8+ T cell activation and tumor immune evasion.* J Clin Invest, 2018. **128**(12): p. 5549-5560.

53. Olah, M., V. Menon, N. Habib, M.F. Taga, Y. Ma, C.J. Yung, M. Cimpean, A. Khairallah, G. Coronas-Samano, R. Sankowski, D. Grün, A.A. Kroshilina, D. Dionne, R.A. Sarkis, G.R. Cosgrove, J. Helgager, J.A. Golden, P.B. Pennell, M. Prinz, J.P.G. Vonsattel, A.F. Teich, J.A. Schneider, D.A. Bennett, A. Regev, W. Elyaman, E.M. Bradshaw, and P.L. De Jager, *Single cell RNA sequencing of human microglia uncovers a subset associated with Alzheimer's disease.* Nature Communications, 2020. **11**(1): p. 6129.

54. Shekarian, T., C.P. Zinner, E.M. Bartoszek, W. Duchemin, A.T. Wachnowicz, S. Hogan, M.M. Etter, J. Flammer, C. Paganetti, T.A. Martins, P. Schmassmann, S. Zanganeh, F. Le Goff, M.G. Muraro, M.-F. Ritz, D. Phillips, S.S. Bhate, G.L. Barlow, G.P. Nolan, C.M. Schürch, and G. Hutter, *Immunotherapy of glioblastoma explants induces interferon-γ responses and spatial immune cell rearrangements in tumor center, but not periphery.* Science Advances, 2022. **8**(26): p. eabn9440.

55. Smolders, J., K.M. Heutinck, N.L. Fransen, E.B.M. Remmerswaal, P. Hombrink, I.J.M. ten Berge, R.A.W. van Lier, I. Huitinga, and J. Hamann, *Tissue-resident memory T cells populate the human brain.* Nature Communications, 2018. **9**(1): p. 4593.

56. Kumar, B.V., W. Ma, M. Miron, T. Granot, R.S. Guyer, D.J. Carpenter, T. Senda, X. Sun, S.H. Ho, H. Lerner, A.L. Friedman, Y. Shen, and D.L. Farber, *Human Tissue-Resident Memory T Cells Are Defined by Core Transcriptional and Functional Signatures in Lymphoid and Mucosal Sites.* Cell Rep, 2017. **20**(12): p. 2921-2934.

57. Mackay, L.K., A. Rahimpour, J.Z. Ma, N. Collins, A.T. Stock, M.L. Hafon, J. Vega-Ramos, P. Lauzurica, S.N. Mueller, T. Stefanovic, D.C. Tscharke, W.R. Heath, M. Inouye, F.R. Carbone, and T. Gebhardt, *The developmental pathway for CD103(+)CD8+ tissue-resident memory T cells of skin.* Nat Immunol, 2013. **14**(12): p. 1294-301.

58. Gandoglia, I., F. Ivaldi, P. Carrega, E. Armentani, G. Ferlazzo, G. Mancardi, N. Kerlero de Rosbo, A. Uccelli, and A. Laroni, *In vitro VLA-4 blockade results in an impaired NK cell-mediated immune surveillance against melanoma.* Immunology Letters, 2017. **181**: p. 109-115.

59. Sankowski, R., C. Böttcher, T. Masuda, L. Geirsdottir, Sagar, E. Sindram, T. Seredenina, A. Muhs, C. Scheiwe, M.J. Shah, D.H. Heiland, O. Schnell, D. Grün, J. Priller, and M. Prinz, *Mapping microglia states in the human brain through the integration of high-dimensional techniques.* Nature Neuroscience, 2019. **22**(12): p. 2098-2110.

60. Kilian, M., R. Sheinin, C.L. Tan, M. Friedrich, C. Krämer, A. Kaminitz, K. Sanghvi, K. Lindner, Y.-C. Chih, F. Cichon, B. Richter, S. Jung, K. Jähne, M. Ratliff, R.M. Prins, N. Etminan, A. von Deimling, W. Wick, A. Madi, L. Bunse, and M. Platten, *MHC class II-restricted antigen presentation is required to prevent dysfunction of cytotoxic T cells by blood-borne myeloids in brain tumors.* Cancer Cell, 2023. **41**(2): p. 235-251.e9.

61. Srivastava, A., L. Malik, T. Smith, I. Sudbery, and R. Patro, *Alevin efficiently estimates accurate gene abundances from dscRNA-seq data.* Genome Biol, 2019. **20**(1): p. 65.

62. Griffiths, J.A., A.C. Richard, K. Bach, A.T.L. Lun, and J.C. Marioni, *Detection and removal of barcode swapping in single-cell RNA-seq data.* Nat Commun, 2018. **9**(1): p. 2667.

63. Lun, A.T.L., S. Riesenfeld, T. Andrews, T.P. Dao, T. Gomes, J. participants in the 1st Human Cell Atlas, and J.C. Marioni, *EmptyDrops: distinguishing cells from empty droplets in droplet-based single-cell RNA sequencing data.* Genome Biol, 2019. **20**(1): p. 63.

64. Vallejos, C.A., D. Risso, A. Scialdone, S. Dudoit, and J.C. Marioni, *Normalizing single-cell RNA sequencing data: challenges and opportunities.* Nat Meth, 2017. **14**(6): p. 565-571.

65. Lun, A., D. McCarthy, and J. Marioni, *A step-by-step workflow for low-level analysis of single-cell RNA-seq data with Bioconductor [version 2; referees: 3 approved, 2 approved with reservations].* F1000Research, 2016. **5**(2122).

66. McCarthy, D.J., K.R. Campbell, Q.F. Wills, and A.T.L. Lun, *Scater: pre-processing, quality control, normalization and visualization of single-cell RNA-seq data in R.* Bioinformatics, 2017. **33**(8): p. 1179-1186.

67. Amezquita, R.A., A.T.L. Lun, E. Becht, V.J. Carey, L.N. Carpp, L. Geistlinger, F. Martini, K. Rue-Albrecht, D. Risso, C. Soneson, L. Waldron, H. Pages, M.L. Smith, W. Huber, M. Morgan, R. Gottardo, and S.C. Hicks, *Orchestrating single-cell analysis with Bioconductor.* Nat Methods, 2019.

68. Lun, A.T., D.J. McCarthy, and J.C. Marioni, *A step-by-step workflow for low-level analysis of single-cell RNA-seq data with Bioconductor.* F1000Res, 2016. **5**: p. 2122.

69. Lütge, A., J. Zyprych-Walczak, U. Brykczynska Kunzmann, H.L. Crowell, D. Calini, D. Malhotra, C. Soneson, and M.D. Robinson, *CellMixS: quantifying and visualizing batch effects in single-cell RNA-seq data.* Life Science Alliance, 2021. **4**(6): p. e202001004.

70. Murtagh, F. and P. Legendre, *Ward's Hierarchical Agglomerative Clustering Method: Which Algorithms Implement Ward's Criterion?* J. Classif., 2014. **31**(3): p. 274–295.

71. Langfelder, P., B. Zhang, and S. Horvath, *Defining clusters from a hierarchical cluster tree: the Dynamic Tree Cut package for R.* Bioinformatics, 2008. **24**(5): p. 719-20.

72. Hao, Y., S. Hao, E. Andersen-Nissen, W.M. Mauck, S. Zheng, A. Butler, M.J. Lee, A.J. Wilk, C. Darby, M. Zager, P. Hoffman, M. Stoeckius, E. Papalexi, E.P. Mimitou, J. Jain, A. Srivastava, T. Stuart, L.M. Fleming, B. Yeung, A.J. Rogers, J.M. McElrath, C.A. Blish, R. Gottardo, P. Smibert, and R. Satija, *Integrated analysis of multimodal single-cell data.* Cell, 2021. **184**(13): p. 3573-3587.e29.

73. Aran, D., A.P. Looney, L. Liu, E. Wu, V. Fong, A. Hsu, S. Chak, R.P. Naikawadi, P.J. Wolters, A.R. Abate, A.J. Butte, and M. Bhattacharya, *Reference-based analysis of lung single-cell sequencing reveals a transitional profibrotic macrophage.* Nat Immunol, 2019. **20**(2): p. 163-172.

74. Law, C.W., Y. Chen, W. Shi, and G.K. Smyth, *voom: precision weights unlock linear model analysis tools for RNA-seq read counts.* Genome Biology, 2014. **15**(2): p. R29.

75. Weber, L.M., M. Nowicka, C. Soneson, and M.D. Robinson, *diffcyt: Differential discovery in high-dimensional cytometry via high-resolution clustering.* Communications Biology, 2019. **2**(1): p. 183.

76. Dann, E., N.C. Henderson, S.A. Teichmann, M.D. Morgan, and J.C. Marioni, *Differential abundance testing on single-cell data using k-nearest neighbor graphs.* Nature Biotechnology, 2022. **40**(2): p. 245-253.

77. Junttila, S., J. Smolander, and L.L. Elo, *Benchmarking methods for detecting differential states between conditions from multi-subject single-cell RNA-seq data.* Briefings in Bioinformatics, 2022. **23**(5).

78. Lun, A.T.L. and J.C. Marioni, *Overcoming confounding plate effects in differential expression analyses of single-cell RNA-seq data.* Biostatistics, 2017. **18**(3): p. 451-464.

79. Robinson, M.D., D.J. McCarthy, and G.K. Smyth, *edgeR: a Bioconductor package for differential expression analysis of digital gene expression data.* Bioinformatics, 2010. **26**(1): p. 139-140.

80. Robinson, M.D. and A. Oshlack, *A scaling normalization method for differential expression analysis of RNA-seq data.* Genome Biol, 2010. **11**(3): p. R25.

81. Love, M.I., W. Huber, and S. Anders, *Moderated estimation of fold change and dispersion for RNA-seq data with DESeq2.* Genome Biology, 2014. **15**(12): p. 550.

82. Wu, D. and G.K. Smyth, *Camera: a competitive gene set test accounting for inter-gene correlation.* Nucleic Acids Res, 2012. **40**(17): p. e133.

83. Subramanian, A., P. Tamayo, V.K. Mootha, S. Mukherjee, B.L. Ebert, M.A. Gillette, A. Paulovich, S.L. Pomeroy, T.R. Golub, E.S. Lander, and J.P. Mesirov, *Gene set enrichment analysis: A knowledge-based approach for interpreting genome-wide expression profiles.* Proc Natl Acad Sci U S A, 2005. **102**(43): p. 15545-15550.

Acknowledgements

We are grateful to the patients and their families for their consent to donate tissue to our brain tumor biobank. We thank Tamara Hüssen, Alison Riberio and Florian Limani for experimental support and Cecile Buenter for critical revision of the manuscript. Calculations were performed at sciCORE (http://scicore.unibas.ch/) scientific computing center at the University of Basel.

Author contribution

G.H., S. Herter, M.B., S.D. and P.S., conceived and planned the project. J.R. and S. Hogan analyzed the scRNA-sequencing data and performed statistical analysis. P.S. and S.D. performed experiments and interpreted the results. T.S., T.A.M. and M.-F.R. helped coordinating experiments. P.S. wrote the manuscript. G.H. supervised and coordinated the study and critically revised the manuscript. All authors reviewed the paper and approved its final version.

Competing interests

G.H. has equity in, and is a cofounder of Incephalo Inc. S.D., S.H. and M.B. are affiliated with Roche Pharmaceutical Research and Early Development. The authors have no financial interests to declare.

980 **Main Figures**

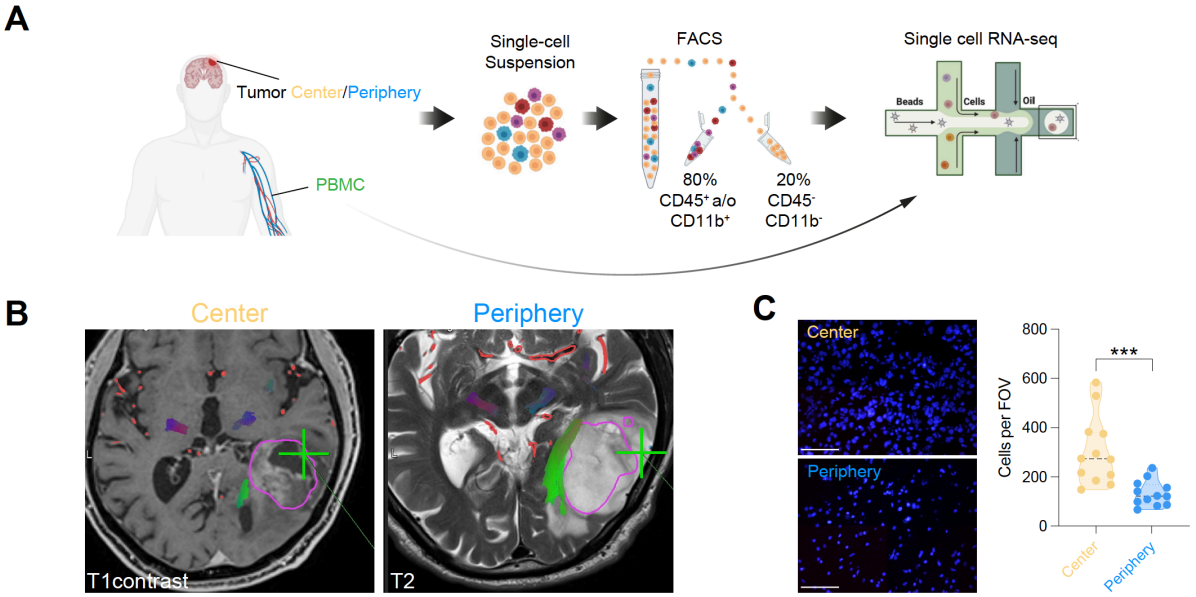

981 **Figure 1 Single-cell RNA-seq of cells from tumor center, periphery and blood.**
982 **(A)** Experimental workflow for single-cell analysis of cells isolated from tumor center, periph-
983 ery and peripheral blood mononuclear cells (PBMC), including fluorescent-activated cell sort-
984 ing and 3'-scRNA-seq. **(B)** Axial T1 with contrast (left) and T2 (right) MRI brain in a patient
985 with a left temporal GBM. Fresh tumor biopsies were taken according to neuronavigation
986 (green cross). The tumor center was defined as contrast enhancing, whereas the tumor periphery
987 was defined as T2 hyperintense. **(C)** Nuclear DAPI staining of resected tissue specimens. 40x
988 magnification (scale bar = 20 µm). n = 3 patients, 4 field of view (FOV) per patient. Statistics:
989 ***$p < 0.001$, two-tailed Mann Whitney U test (Figure 1 – source data 1).

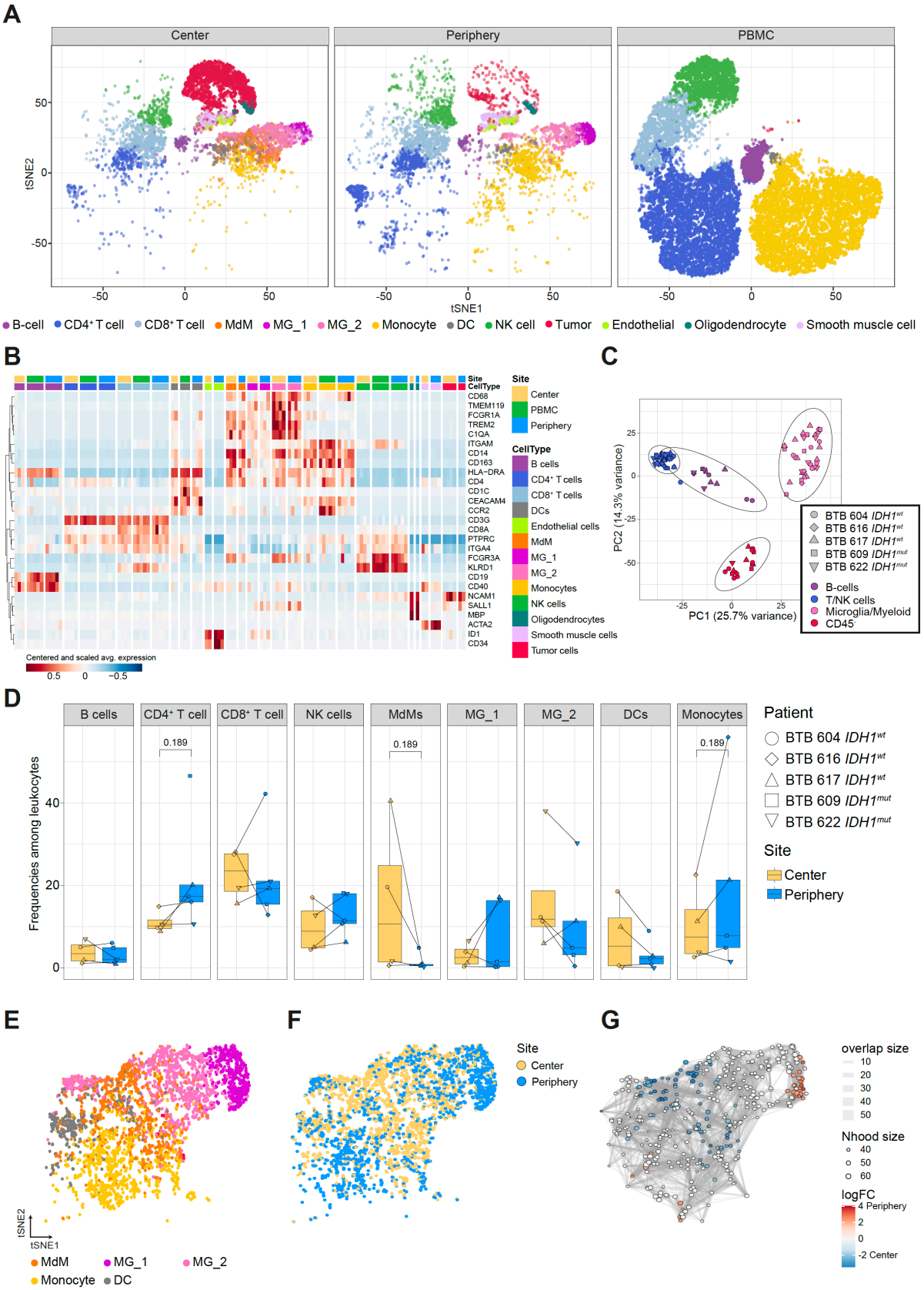

Figure 2 Single-cell RNA-seq analysis identifies main immune cell populations. **(A)** Dimensionally reduced tSNE projection of the scRNAseq data showing the annotated cell types. **(B)** Heatmap displaying centered and scaled normalized average expression values of characteristic cell-type specific genes used to annotate clusters. Columns are ordered by site

995 and cell type, and rows show centered and scaled expression values, hierarchically clustered.
996 Heatmap displaying genes whose expression is most specific to each cell type is shown in Fig-
997 ure 2 – figure supplement 2. (**C**) Principal component analysis of pseudo-bulk scRNAseq sam-
998 ples aggregated by patient and cell type. Symbols represent individual patients and cell lineage
999 is displayed by different colors. (**D**) Relative frequencies of immune populations among leuko-
1000 cytes between tumor center and periphery. Symbols represent individual patients and paired
1001 samples are indicated by connecting lines. *P*-values were calculated using *diffcyt-DA-voom*
1002 method (Figure 2 – source data 1). (**E-G**) Differential abundance testing of the tumor innate
1003 immune compartment (**E**) using the *miloR* package which tests the abundance of each neigh-
1004 borhood of cells separately between tumor center und periphery (**F, G**).

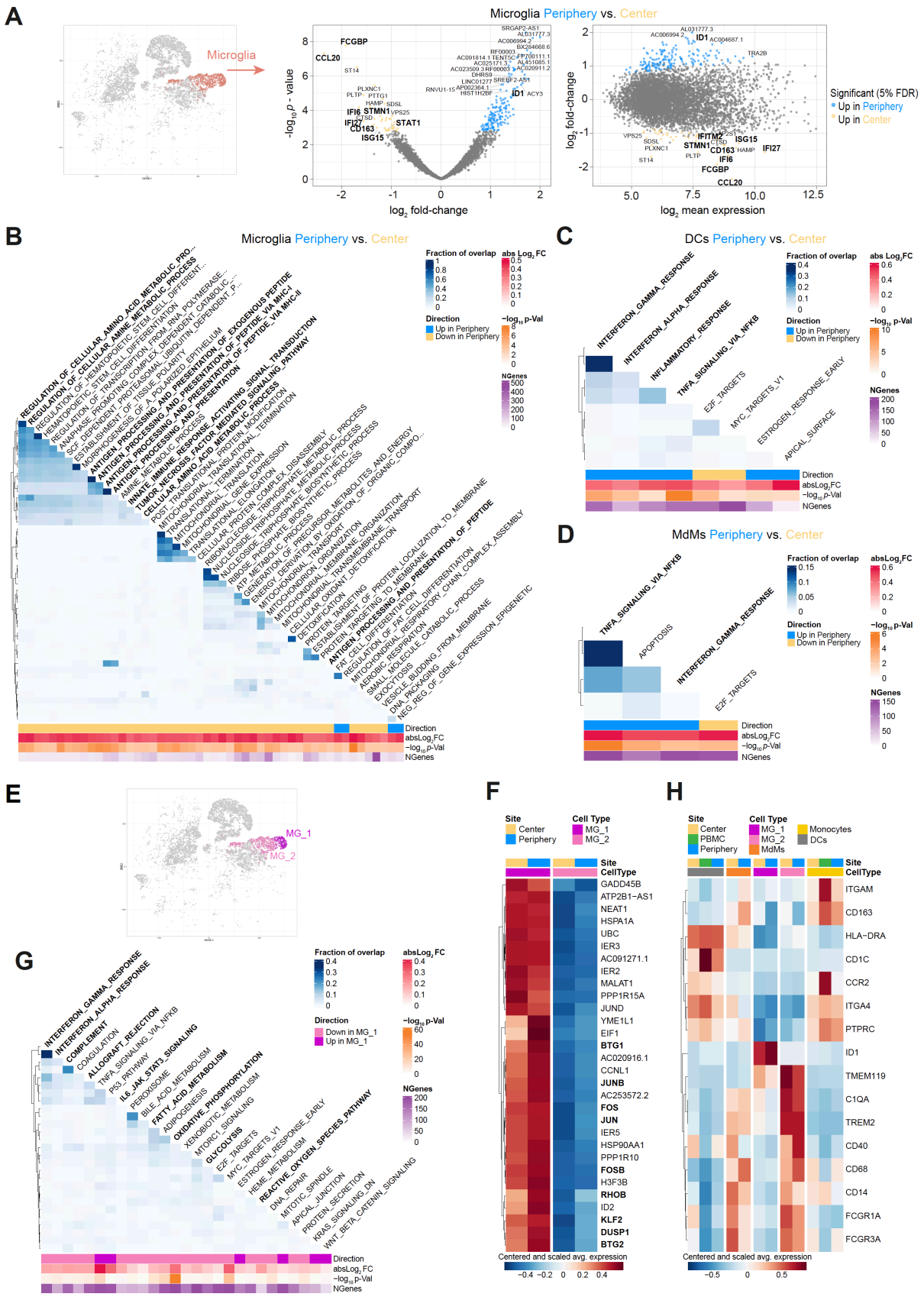

Figure 3 MG display regionally resolved transcriptional profiles that differ from those of DCs and MdMs.

1008 **(A)** Microglia cluster highlighted on tSNE map and scatterplots showing differentially ex-
1009 pressed genes (FDR<5%, indicated by blue and yellow) in Microglia (MG) cells from tumor
1010 periphery versus center. Volcano plot showing *p* value versus fold-change (left) and MA plot
1011 showing fold-change versus mean expression (right). For a complete list of differentially ex-
1012 pressed genes per cell cluster between tumor periphery and center, please refer to Supplemen-
1013 tary File 4. **(B)** Heatmap representation of Gene set enrichment analysis (GSEA) results be-
1014 tween peripheral and center microglia using Gene Ontology (GO) collection (Biological Pro-
1015 cesses). The fraction of overlap between gene sets is calculated as Jaccard coefficient of overlap
1016 between the gene sets. **(C, D)** Heatmap representation of GSEA of DCs **(C)** and monocyte-
1017 derived macrophages (MdMs) **(D)** from tumor periphery versus tumor center using Hallmark
1018 collection of major biological categories. **(E)** Unsupervised hierarchical sub-clustering of the
1019 MG population revealed two transcriptionally distinct subsets of MG, termed MG_1 and
1020 MG_2, displayed on the tSNE map. **(F)** Heatmap displaying the cluster-specific genes identi-
1021 fying MG_1 subcluster. Columns are ordered by site and cell type, and rows show centered and
1022 scaled normalized average expression values, hierarchically clustered. A complete list of cluster
1023 specific genes for MG_1 and MG_2 subcluster is provided in Supplementary File 5. **(G)**
1024 Heatmap representation of GSEA between MG_1 and MG_2 subclusters using Hallmark col-
1025 lection of major biological categories. **(H)** Heatmap displaying previously described reactivity
1026 markers of MG. Columns are ordered by site and cell type, and rows show centered and scaled
1027 normalized average expression values, hierarchically clustered.

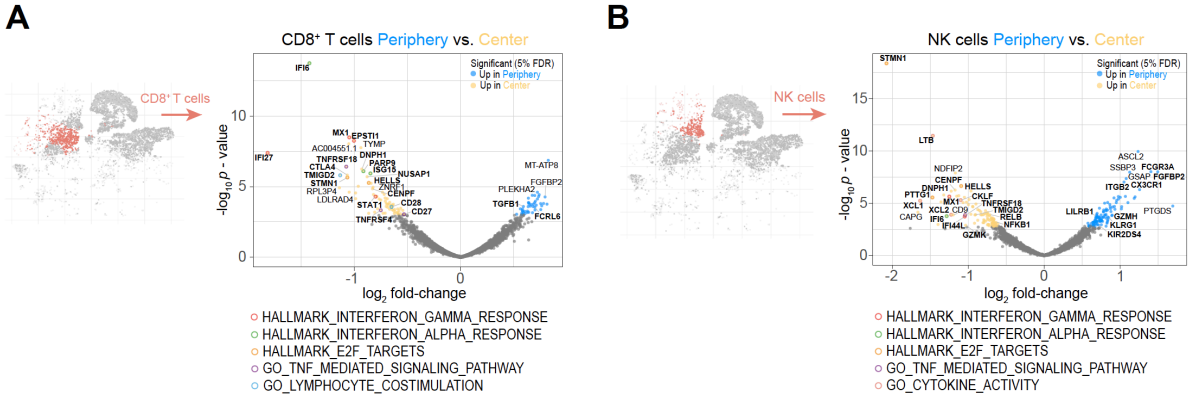

Figure 4 The peripheral cytotoxic cell compartment exhibits an impaired activation signature.

(A, B) Volcano plots showing differentially expressed genes (FDR corrected p value < 0.05, indicated by blue and yellow) in CD8$^+$ T cells (**A**) and NK cells (**B**) from tumor periphery versus tumor center. Colored rings mark genes belonging to selected GSEA Hallmark or Gene Ontology (GO) pathways as indicated. For a complete list of differentially expressed genes per cell cluster between tumor periphery and center, please refer to Supplementary File 4.

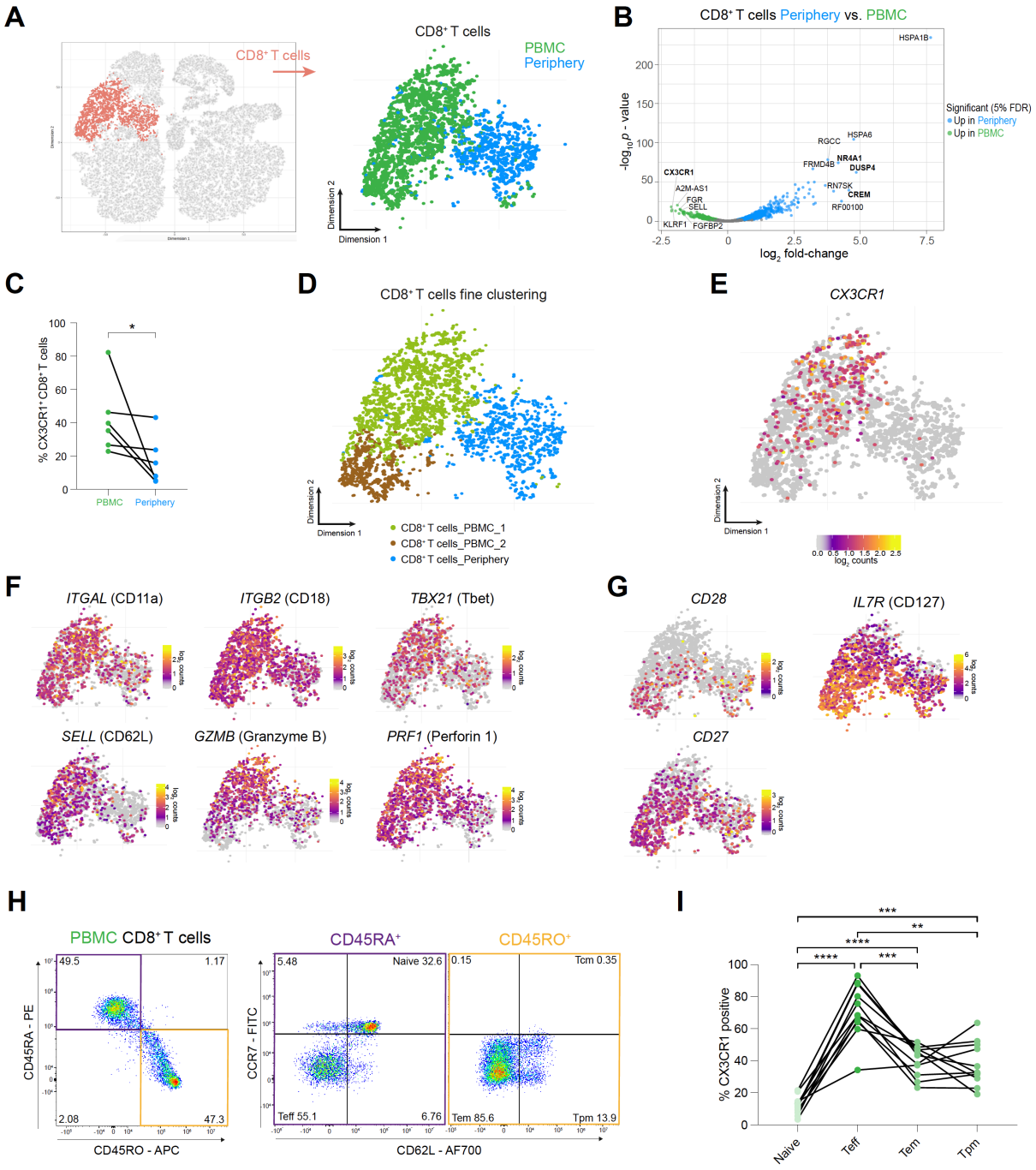

Figure 5 CX3CR1 labels a specific CD8+ T cell population in the circulation of grade 4 glioma patients.

(A) CD8$^+$ T cell cluster highlighted on tSNE map (left). CD8$^+$ T cell cluster colored by site of origin (right). **(B)** Volcano plot showing differentially expressed genes (FDR corrected *p* value < 0.05, indicated by blue and green) in CD8$^+$ T cells from tumor-periphery versus PBMC. For a complete list of differentially expressed genes per cell cluster between tumor periphery and PBMC, please refer to Supplementary File 6. **(C)** Frequency of CX3CR1$^+$ CD8$^+$ T cells among all CD8$^+$ T cells in flow cytometry data (Figure 5 – source data 1). **(D)** Unsupervised hierarchical sub-clustering of CD8$^+$ T cells from PBMC and Periphery revealed two transcriptionally

1046 distinct subsets of PBMC $CD8^+$ T cells, displayed on the tSNE map. (**E)** Expression of *CX3CR1*
1047 overlaid on tSNE $CD8^+$ T cell cluster. (**F)** Expression of genes associated with effector memory
1048 phenotype overlaid on tSNE $CD8^+$ T cell cluster. Displayed genes are significantly, differen-
1049 tially expressed genes (DEGs) between tumor periphery and PBMC, as identified by differen-
1050 tial gene expression analysis shown in panel (B). (**G)** Expression of selected genes associated
1051 with naive phenotype overlaid on tSNE $CD8^+$ T cell cluster (**H)** Gating procedure applied to
1052 identify $CD3^+$ $CD8^+$ naïve, T effector cells (T_{eff}), effector memory (T_{em}), peripheral memory
1053 (T_{pm}) and central memory (T_{cm}), eluted from PBMCs. (**I)** Expression of CX3CR1 in PBMC
1054 $CD8^+$ T cell subpopulations identified in (H) (Figure 5 – source data 2). n = 6 donors (**C**), n =
1055 11 donors (**I**). Statistics: Wilcoxon matched-pairs signed rank test (**C**); repeated measures one-
1056 way ANOVA with post-hoc Šidák's correction for multiple comparisons (**I**). *$p \leq 0.05$, **$p \leq$
1057 0.01, ***$p \leq 0.001$, ****$p \leq 0.0001$, no brackets indicate no significant difference.

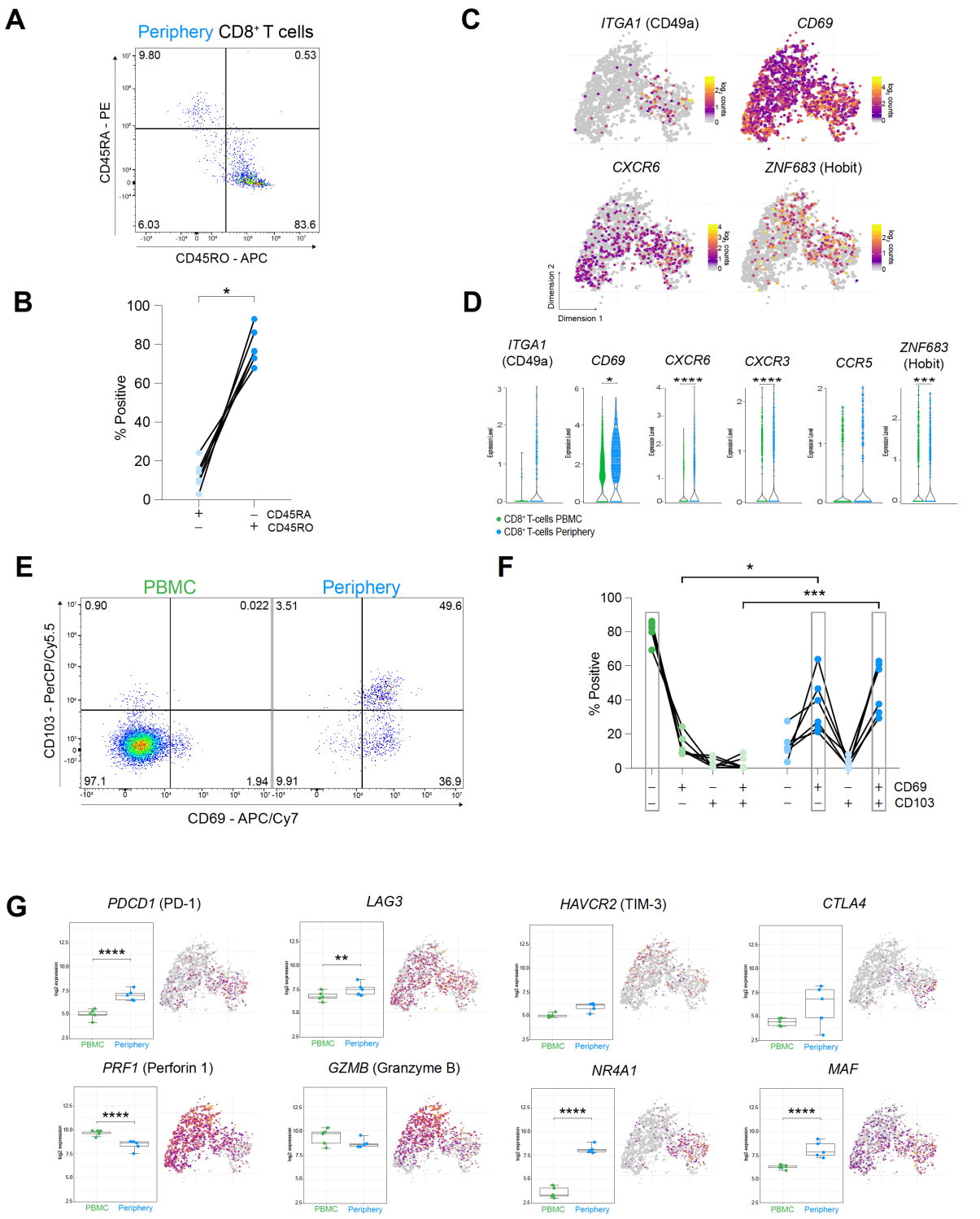

Figure 6 CD8+ T cells in the tumor periphery share features with tissue-resident memory T cells (Trm)

(**A**) Representative dot plot of tumor-periphery CD8+ T cells stained for CD45RA and CD45RO. (**B**) Quantification of tumor-periphery CD8+ T cells expressing CD45RA or CD45RO (Figure 6 – source data 1). (**C**) Expression of genes associated with tissue-resident memory (T_{rm}) phenotype overlaid on tSNE CD8+ T cell cluster. (**D**) Average expression levels of selected T_{rm} markers between CD8+ T cells from PBMC versus tumor-periphery.

1066 Significance testing based on differential gene expression analysis shown in panel (Fig. 5B)
1067 (**E)** Representative dot plots of CD69 and CD103 co-expression in $CD8^+$ T cells from PBMC
1068 and tumor-periphery. (**F)** Quantification of CD69 and CD103 co-expression revealed $CD69^-$
1069 $CD103^-$ in PBMC and $CD69^+$ $CD103^-$ and $CD69^+$ $CD103^+$ in tumor-periphery as the dominant
1070 phenotypes (Figure 6 – source data 2). (**G)** Expression of selected markers associated with T
1071 cell exhaustion/dysfunction, shown as boxplots between $CD8^+$ T cell from PBMC and tumor-
1072 periphery and overlaid on tSNE $CD8^+$ T cell cluster. $n = 6$ donors (**B, F**). Statistics: Wilcoxon
1073 matched-pairs signed rank test (**B**); repeated measures one-way ANOVA with post-hoc Šidák's
1074 correction for multiple comparisons (**F**). *$p \leq 0.05$, **$p \leq 0.01$, ***$p \leq 0.001$, ****$p \leq 0.0001$,
1075 no brackets indicate no significant difference.

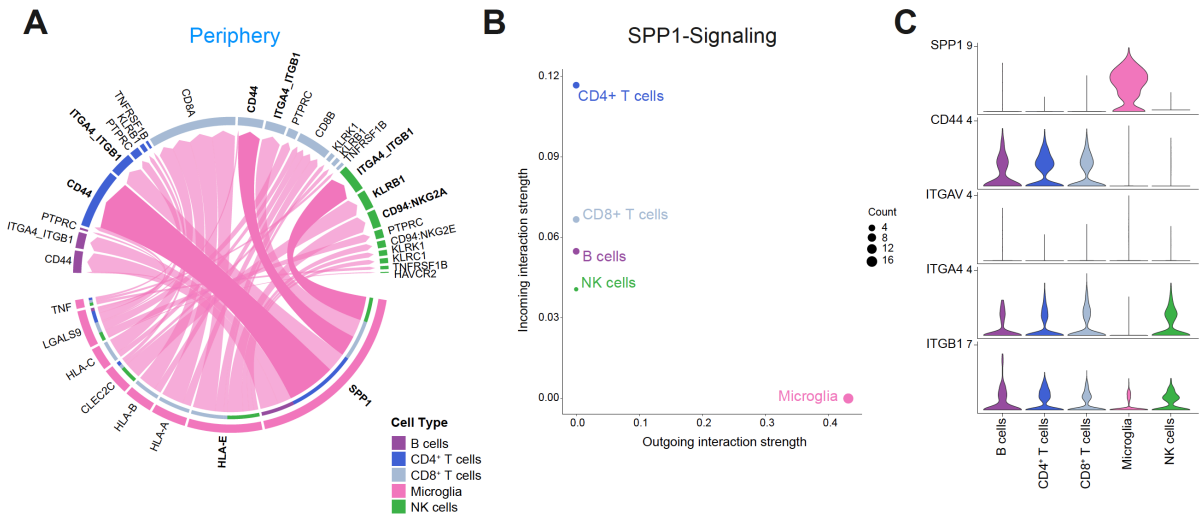

Figure 7 Cell-cell communication analysis using CellChat reveals critical role for SPP1-mediated crosstalk in tumor periphery.

(A) Chord diagram showing significant interactions from microglia to lymphocyte cell clusters. The inner bar colors represent the targets that receive signal from the corresponding outer bar. The inner bar size is proportional to the signal strength received by the targets. Chords indicate ligand-receptor pairs mediating interaction between two cell clusters, size of chords is proportional to signal strength of the given ligand-receptor pair. **(B)** Comparison of incoming and outgoing interaction strength allows identification of main senders and receivers. **(C)** Violin plots showing the expression distribution of signaling genes involved in the inferred SPP1 signaling network.